

Citation for published version:
Tuechler, S & Copeland, C 2019, 'Experimental Results from the Bath -Wave Rotor Turbine Performance Tests',
Journal of Energy Conversion and Management, vol. 189, ECM-D-19-00781, pp. 33-48.
https://doi.org/10.1016/j.enconman.2019.03.079

10.1016/j.enconman.2019.03.079

Publication date: 2019

Document Version Peer reviewed version

Link to publication

Publisher Rights CC BY-NC-ND

University of Bath

Alternative formats

If you require this document in an alternative format, please contact: openaccess@bath.ac.uk

General rights

Copyright and moral rights for the publications made accessible in the public portal are retained by the authors and/or other copyright owners and it is a condition of accessing publications that users recognise and abide by the legal requirements associated with these rights.

If you believe that this document breaches copyright please contact us providing details, and we will remove access to the work immediately and investigate your claim.

Download date: 09. Mar. 2023

Draft: Experimental Results from the Bath μ -Wave Rotor Turbine Performance Tests

Stefan Tüchler^{a,*}, Colin D. Copeland^a

^aPowertrain and Vehicle Research Centre, Department of Mechanical Engineering, University of Bath, Claverton Down, Bath BA2 7AY, United Kingdom

Abstract

This paper details an extensive experimental investigation of a novel throughflow micro-wave rotor with symmetrically cambered passage profiles designed for shaft power output as well as pressure exchange. This is the first time comprehensive experimental data from a power generating wave rotor is presented in a peer-reviewed journal. Moreover, the significance and renewed interest in wave rotors for a wide range of applications from refrigeration to micro-gas turbines makes this experimental programme extremely valuable to many fields of research.

The wave rotor is a four port, three-cycle unit of 60 mm in diameter, 30 mm in length and houses 46 channels. The unit was experimentally tested on a gas stand in open-loop configuration using electrical heaters as a source of heat for the high pressure inlet and pressurised air for both inlet ducts. Throughout testing, the mass flow rates among high pressure in- and outlet were balanced.

A series of tests were conducted investigating the effect of variation in rotational speed, ratio of inlet mass flow rates (loop flow ratio), axial clearances and peak inlet temperature on wave rotor performance. The results show the importance of minimum axial clearance for maximum energy transfer as well as for reduced mixing of hot and cold flows. The competing relationship between pressure ratio, high pressure zone pressure difference, internal exhaust gas recirculation and fresh air exhaustion is also highlighted. Finally, measurements of the temperature distributions in the high pressure outflow show the effect of rotational speed, loop flow ratio and centrifugal forces on the fresh air stream location and its mixing with the hot gas stream.

A peak shaft power of 450 W and a peak pressure ratio of approximately 1.63 were obtained close to the design speed that were in line with expectations for clear-

Email address: S.Tuechler@bath.ac.uk (Stefan Tüchler)

^{*}Corresponding author

ances and temperatures under investigation. Using a new approach to calculating efficiency that assumes equal values for expansion and compression, a peak figure of 80% was obtained indicating the superiority that such designs have over similarly sized traditional turbomachinery.

Keywords: Wave rotor turbine, Wave action, Experimental testing, Pressure exchange

NΤ		~~~	1.4	
IN	om	enc	ıat	ure

 ΔT Temperature difference [K]

 c_p Specific heat capacity at constant ν Kinematic viscosity [m²/s]

pressure [J/kg-K]

A Cross-section area [m²]

D Diameter [m]

F Non-dim. friction [-]

G Non-dim. leakage [-]

L Length [m]

M Mach number [-]

R Specific gas constant [J/kg-K]

T Temperature [K], non-dim. finite

passage opening[-]

U Tangential velocity [m/s]

 \dot{m} Mass flow rate [kg/s]

a Speed of sound [m/s]

h Height [m]

t Time [s]

w Width [m]

z Axial coordinate [m]

Π Pressure ratio [-]

 Ψ EGR rate [-]

 β Blade angle [°]

 δ Leakage gap [m]

 η Efficiency [-]

 γ Ratio of specific heats [-]

 λ Loop flow ratio [-]

 ω Angular speed [rad/s]

 θ Angular coordinate [rad]

EGR Exhaust gas recirculation

FAE Fresh air exhaustion

FS Full scale

HPA High pressure air

HPG High pressure gas

LPA Low pressure air

LPG Low pressure gas

PE Pressure exchanger

PWS Pressure wave supercharger

RF Reverse flow

SLM Selective laser melting

TF Throughflow

c Cold, compression

ch Channel

h Hydraulic, hot

is Isentropic

m Mixed

s Static

t Total

x Expansion

1. Introduction

2 1.1. Background and Operating Principle

Wave rotors are a type of dynamic pressure exchange machinery, where energy is transferred through shock waves. The technology bears the potential to further enhance thermal cycles and thus reduce global energy consumption and increase thermodynamic efficiency. As a result, wave rotors have been suggested in a range of fields of application, ranging from pressure gain combustors [1, 2], to gas turbine topping cycles [3, 4], wave rotor turbines [5], pressure wave superchargers for internal combustion engines [6, 7] and refrigeration cycles [8, 9], as summarised in Figure 1.

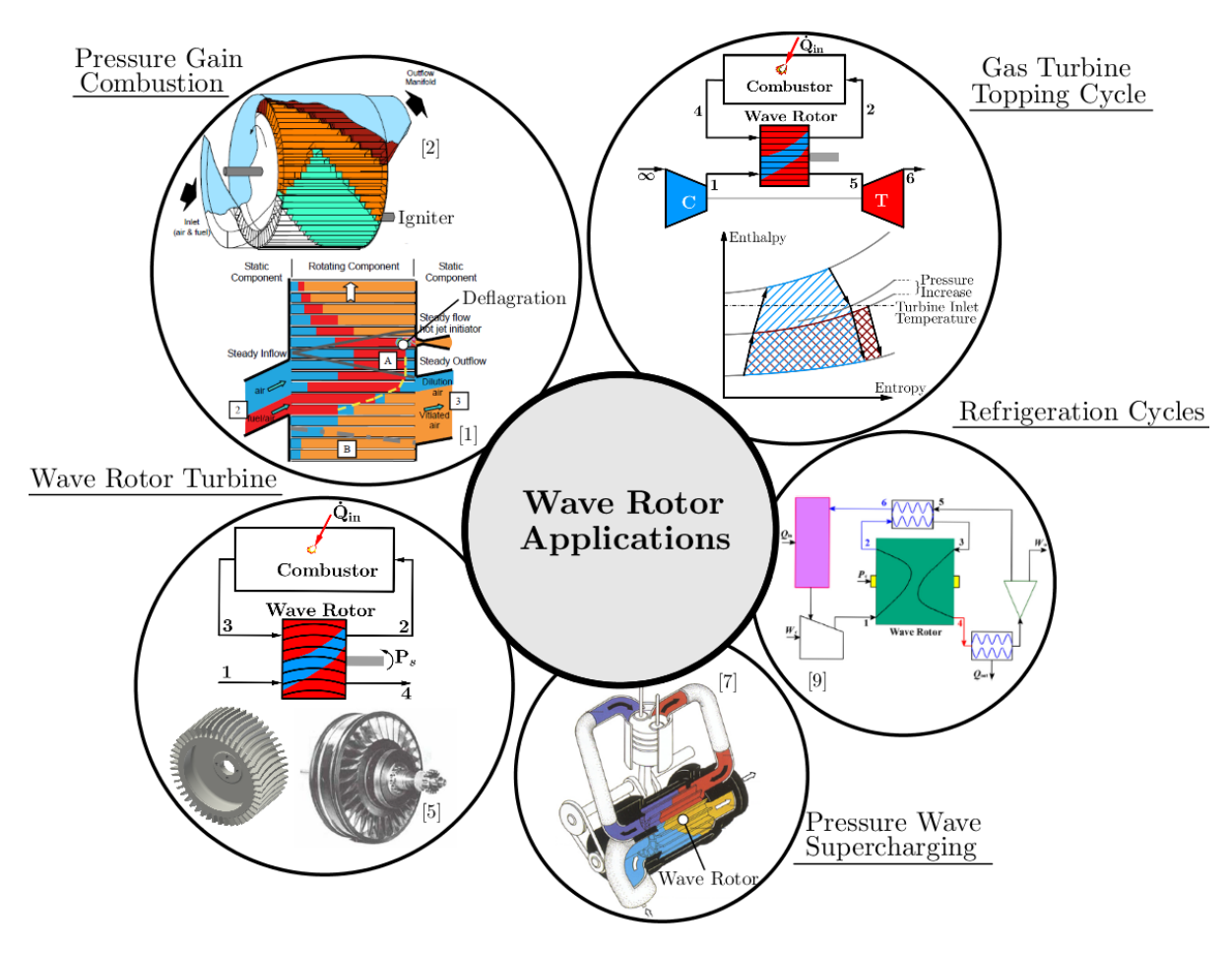


Figure 1: Summary of wave rotor applications aimed at enhancing thermal cycles and reducing energy consumption. These range from gas turbine enhancement through pressure gain combustion [1, 2], topping cycles [3, 4] and wave rotor turbines [5]. Furthermore, wave rotors can be applied to internal combustion engines as a supercharging device [6, 7] and to refrigeration cycles [8, 9].

The principle involves shock and expansion waves travel along discrete channels arranged around the circumference of a cylindrical drum. This process is unsteady and does not require additional moving parts. To each side of the rotor, there are stator endplates containing port openings, as shown in Figure 2(a). The rotor channels are then periodically exposed to the thermodynamic conditions in the ports triggering the generation of shock and expansion waves. Introducing channel camber and an angled arrangement of inlet and outlet ports additionally allows to employ the wave rotor as a turbine for shaft power extraction.

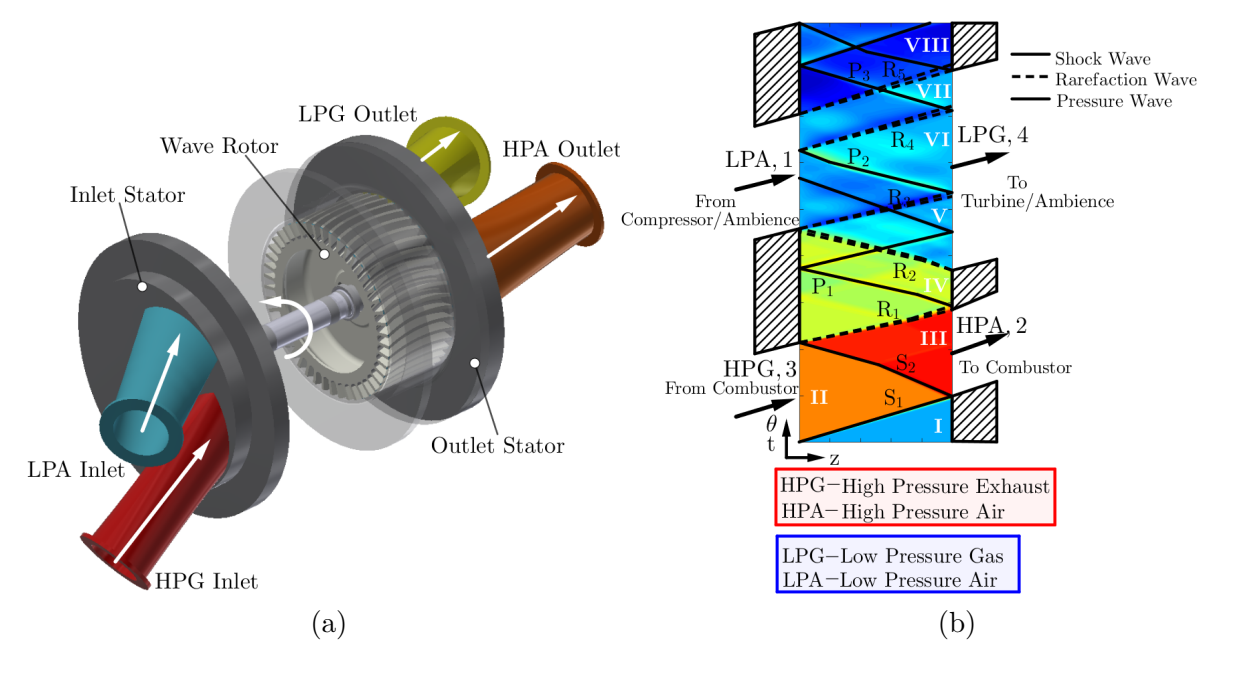


Figure 2: (a) Main components of a generic four-port, single cycle throughflow wave rotor consisting of inlet and outlet stator endplates and rotor/bearing assembly. (b) Unfolded view of the wave pattern experienced as a single channel passes through the port arrangement of a four-port throughflow wave rotor showed in the θ -z plane.

In order to examine the wave action processes taking place within a single channel, one can examine the unwrapped wave pattern on a two-dimensional θ -z-plane, as done in Figure 2(b). The device features two high pressure ports, namely a high pressure exhaust gas (HPG) and high pressure air (HPA), that form the combustor loop. It further shows two low pressure ports, the low pressure air intake (LPA), from where the fresh air is drawn-either from ambience or from an upstream compressorinto the rotor, and the low pressure gas port (LPG), through which the hot exhaust gases are expelled to the ambience or alternatively further expanded by a turbine.

Initially, pressure and temperature within the channels are close to ambient conditions. Exposing the channel to the left with the high pressure, high temperature exhaust gas from the combustor (HPG) sets off a right travelling, primary shock wave (S1). Upon reaching the other end of the channel the HPA port is opened and the shock wave is reflected resulting in a secondary, left running shock wave (S2). These two shock waves compress the incoming fresh air and their strength governs the compression ratio achieved by the rotor.

Closing the HPG port sparks an expansion fan or rarefaction wave (R1), which expands the exhaust gases to an intermediate pressure level. Impingement of the head of R1 on the right hand side marks the closure of the HPA port, which prompts a hammer shock like pressure wave (P1). Opening the low pressure exhaust port (LPG) leads to further expansion of the gases (R2) before the gases are ejected to the ambience. The low pressure inlet port opens as soon as (R2) reaches the left hand side of the channel. Finally, closure of the LPA port generates weak pressure waves before the cycle is repeated.

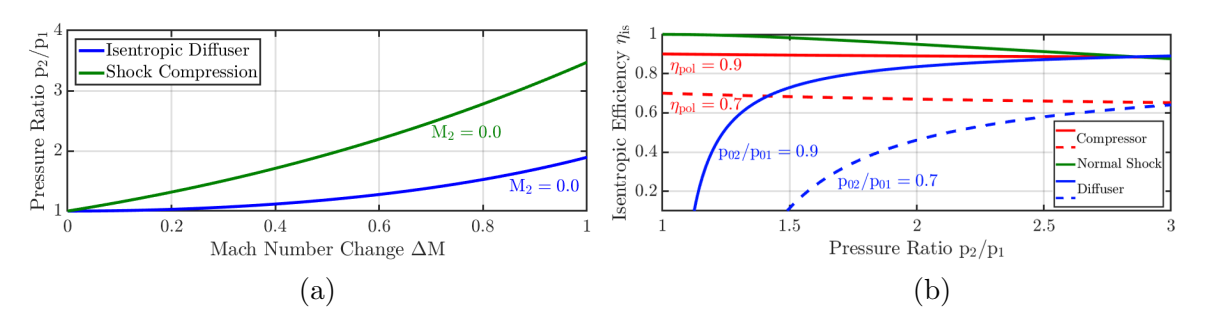


Figure 3: (a) Static pressure ratio plotted versus Mach number change for steady (diffuser - lower, blue curve) and unsteady (moving, normal shock wave-upper green curve) compression (amended from [10]). (b) Isentropic efficiency plotted versus static pressure ratio for compressor (red curves), diffuser (blue curve) and shock compression (green curve) (amended from [11]).

The geometry of a wave rotor does not feature any complex surfaces and comprises simple channel shapes. Due to the presence of both the hot expanded gas stream and the cold air stream the wave rotor is inherently self-cooled and the material temperature remains below the peak cycle temperature. Another distinct advantage of unsteady flow devices over steady, such as diffusers, or crypto-steady flow devices (compressor/turbine turbomachinery arrangement) is illustrated in the graphs of Figure 3. In comparison with steady flow devices (lower, blue curve in Fig. 3(a)) and assuming the Mach number downstream is reduced to zero, shock compression (top, green curve) as witnessed in a wave rotor accounts for a larger static pressure ratio for any given Mach number change. Furthermore, as diffusers become large in

size to prevent undesired flow separation, compression in an unsteady fashion yields higher pressure ratios over a smaller distance.

Looking at the isentropic efficiency in Fig. 3(b) and comparing compression through a moving shock without wall friction (solid green line), a compressor (blue lines) with different polytropic efficiencies (0.9 and 0.7) and diffusers (red lines) with different total pressure loss (0.1 and 0.3) considered, it becomes apparent that for static pressure ratios of approximately three, unsteady compression features higher isentropic efficiency. This signifies that for the same pressure ratio, several stages of diffusion or increases in kinetic energy are necessary to obtain the same pressure ratio. As a result, unsteady devices can be built compact. Nonetheless, it should be added that wall friction and potential shock-boundary layer interaction would reduce shock efficiency.

1.2. Literature Survey

52

53

57

61

63

64

68

73

74

79

81

Over the past decades numerous research studies from a variety of research institutes have been dedicated towards the investigation of dynamic pressure exchange machinery, such as wave rotors. Early research efforts aimed at introducing pressure exchangers of straight channel profiles as a means to enhance gas turbine cycles [3, 4, 12] and internal combustion engines [6, 7, 13, 14]. More recent studies further pursue gas turbine [15–18] and reciprocating engine [14, 19, 19–22] enhancement. In addition, the field of applications has been extended through the application of wave rotors in refrigeration cycles [8, 9, 23–26] and pressure-gain combustors [1, 2, 27– 33. In comparison with the amount of numerical research on wave rotor design and performance, there are relatively few studies dedicated to the experimental characterisation of wave rotors. The bulk of them were conducted at NASA Glenn Research Center. Initial studies were done predominantly on pressure exchangers and equalisers, where temperatures are generally low. One of the first studies was conducted by Kentfield at Imperial College London [34, 35] on a rotor of an approximately 200 mm diameter rotor spinning at 6000 rpm with a focus performance and efficiency maps of pressure divider and equaliser. The effect of leakage variation on the achieved pressure ratios of a pressure divider was investigated by Wilson and Fronek [36] implying a linear relationship between axial clearance and pressure ratio. A follow-up study further investigated the effects of friction and finite opening timing and determined a squared relationship between efficiency, friction factor and finite opening timing factor, respectively. A four-port throughflow wave rotor suitable for usage in a gas turbine topping cycle was experimentally characterised by Wilson et al. [37, 38]. The tests were conducted with a chilled air supply for the LPA inlet, limiting the necessary heat supplied by the heater. Sweeps of inlet mass flow rate, loop flow ratio were conducted and the sensitivity of the low pressure section pressure p4/p1 and temperature ratios T4/T1 to variations investigated. Most recent experimental work carried out by the US Air Force Research Laboratory by Mataczynski et al.[14, 20, 39], McClearn et al. [40, 41], Lapp et al.[19] and Reinhart et al. [22]. The first set of studies dealt with a four-port reverse flow pressure wave supercharger for downsized ICE engines. The rotor was designed for a rotational speed of 34,500 rpm and had a mean diameter of 34 mm. The tests yielded promising result, despite suffering from rotor dynamic and premature bearing failures due to insufficient bearing sealing. This limited the peak cycle temperature to around 360°C. Both McClearn et al. [40, 41] and Lapp et al. [19] used an external combustor in their wave rotor testing providing a peak cycle temperature of around 840°C. The former study investigated a small-scale rotor of 42 mm in diameter and a target rotational speed of 38,500 rpm with a target exhaust power of 1.8 kW, while the rotor of the latter study measured 36 mm in diameter and had a target rotational speed of 60,000 rpm delivering an exhaust stream power of 500W. Reinhart et al. [22] tested a small scale wave rotor and coupled the wave rotor to a compression ignition engine examining the effect of the small-scale pressure-wave supercharger on engine performance.

89

90

91

100

101

102

103

104

105

106

107

108

109

110

111

112

113

114

115

116

117

118

119

120

121

122

123

124

All of the mentioned studies deal with straight channels. There are, however, few studies in the public domain on cambered profiles. These wave rotor turbines with cambered passage walls aim at acting both as pressure exchangers while producing shaft power through momentum change of the flow. Most efforts date back to the late 20th century and, unfortunately, documentation of these endeavours is fragmentary. Pearson [5, 42] carried out successful tests at the University of Bath on a single cycle, through-flow wave rotor with helical passage shape leading to a power output of around 26 kW at a rotational speed of 18,000 rpm. The machine achieved a thermal efficiency of approximately 10 % before being subsequently destroyed as a result of overspeeding, which resulted in suspension of the project. Other efforts by General Electric and General Power Corporation were also ceased as the generated shaft power output was deemed insufficient [43, 44]. Piechna et al. introduced a radial, reverse flow wave-disk engine that uses shock-waves and curved channels to create shaft power and energy exchange. The concept has been extensively investigated through numerical means [45–48] and although an experimental facility was introduced [49] and filed for patent [50], no experimental results have thus far been reported in the open literature.

This paper aims at addressing this gap by presenting a small scale wave rotor turbine with symmetrically cambered profiles that enable shaft power output of approximately 400-500W at a design speed of 32,000 rpm while performing as a pressure

exchanging device. To the authors' knowledge, this is the first time detailed experimental results of a power generating wave rotor turbine are presented. This study therefore aims to make an important contribution to the body of knowledge in-so-far as to share quantitative evidence both of the enormous potential that wave rotors offer but some of their unique operating characteristics and challenges as well. It will demonstrate experimentally how efficient shock compression and shaft power can be achieved in a relatively simple design through the shock expansion of a hot gas. What is more, given the small size of the test device, this can be accomplished at a fraction of the rotation speed of more traditional turbomachinery. However, a wave rotor is subject to internal fluid heat and mass exchange and is sensitive to the stator-rotor gap.

The structure of the paper is thus as follows: Firstly, performance parameters of wave rotors are presented before the design including stationary and rotational components is introduced and a comparison of the rotor with other examples with respect to friction, finite opening time and leakage is done. This is followed by an introduction of the experimental setup, instrumentation and the scope of experimental tests. After that ensues a discussion of experimental results including issues faced during testing, before conclusions are drawn.

2. Methodology

2.1. Performance Parameters

The investigated wave rotor is a four-port throughflow design, where wave action accommodates for compression and expansion of the working fluid. Figure 4(a) indicates these shock and expansion waves as well as the distribution of fresh and hot gases through the wave rotor cycle near design conditions. As previously stated, hot gases enter through the HPG port, while fresh air enters through the LPA port. Generally, the mass flow rates through these two inlet ports $\dot{m}_{\rm HPG}$ and $\dot{m}_{\rm LPA}$ are unequal and vary depending on operating conditions.

The ratio of the inlet mass flow rates is referred to as loop flow ratio λ , as seen in Equation 1.

$$\lambda = \frac{\dot{m}_{\rm HPG}}{\dot{m}_{\rm LPA}} \tag{1}$$

Mass flow rates entering through HPG and LPA ports respectively is governed by the stagnation properties in the corresponding ports and back pressure on the outlet side. Variation in λ for a given $\dot{m}_{\rm HPG}$ will determine the mass entering through the

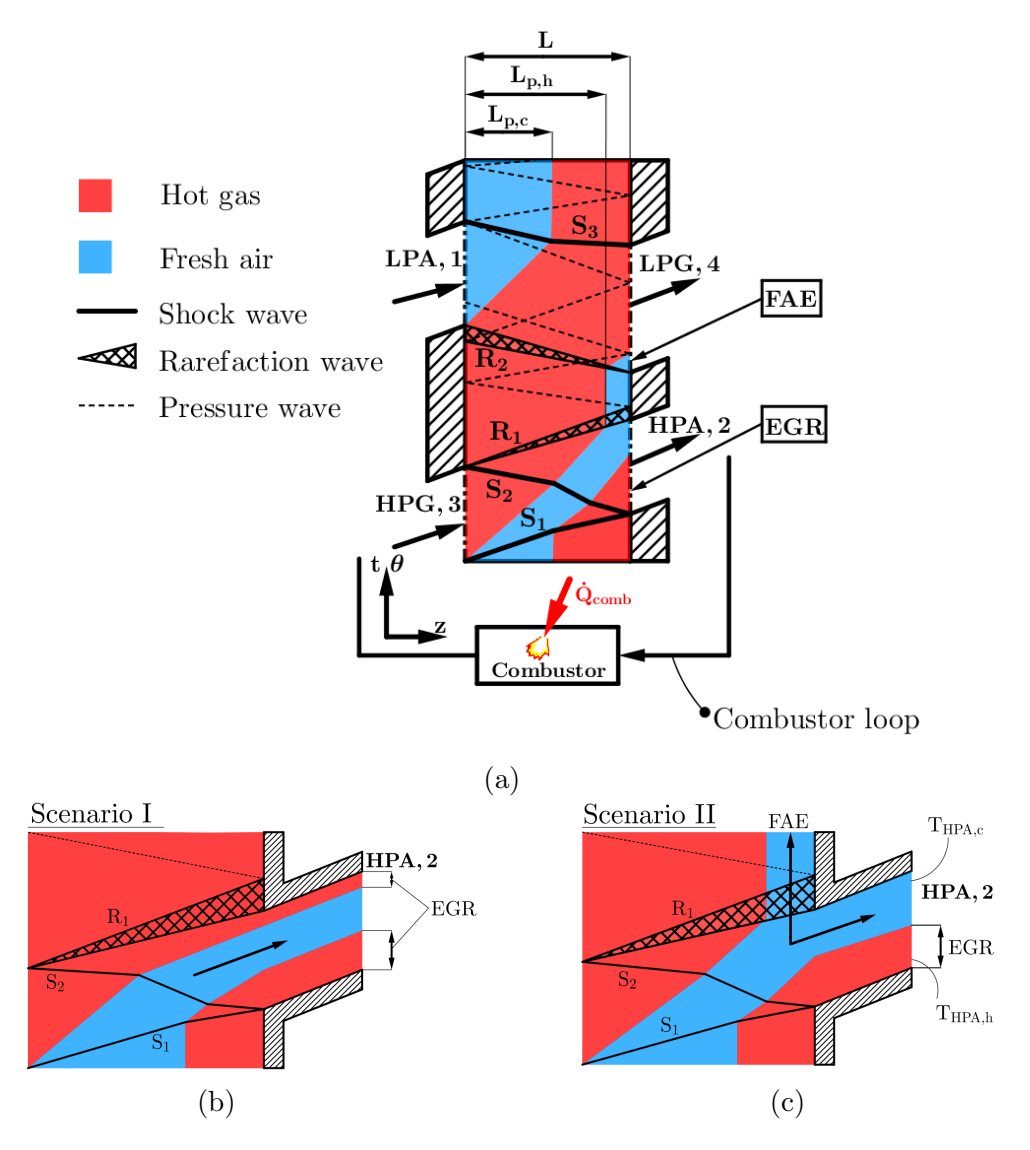


Figure 4: (a) Wave rotor cycle schematic showing general distribution of fresh and hot exhaust gases within the rotor leading to fresh air exhaustion (FAE) through the LPG port and exhaust gas recirculation (EGR) through the HPA port. The amount of EGR and FAE are a function of the hot and cold mass flow rates. (b) shows a closeup of a scenario including solely EGR without FAE while (c) depicts a situation, where both EGR and FAE occur.

LPA port and thus define the penetration length $L_{p,c}$ of the fresh air into the channel. Operating at moderately elevated pressures results in a $L_{p,c}/L$ of approximately 0.5. This signifies that there will be a certain amount of hot gases that do not leave the domain through the LPG port, but are carried over through the HPA port. This inherent characteristic of wave rotors is referred to as exhaust gas recirculation (EGR).

The hot gas penetration length $L_{p,h}$ is considerably greater than its cold air correspondent, due to the generally higher mass flow rate. However, depending on the thermodynamic conditions in the port and the rotational speed of the rotor it may be that it is not sufficient to scavenge the entire channel- such as is the case in scenario I in Figure 4(a)- resulting in some fresh air remaining within the channel after it has passed the HPA port exit. This fresh air is then transferred and expelled unused through the LPG port, resulting in fresh air exhaustion (FAE). This corresponds to scenario II shown in Figure 4(b).

Defining efficiency is more problematic for wave rotors compared to traditional turbomachinery. The traditional enthalpy based efficiency definition assumes adiabatic conditions and thus yields erroneous values with compression efficiency being considerably under- and expansion efficiency overpredicted with values greater than 1. This is caused by the fact that both the hot expanded gas stream and the colder compressed air stream are transported within the same channels and thus in direct contact with each other. This gives rise to heat exchange between the two streams, which acts as an internal recuperator, but renders a consistent definition of wave rotor compression and expansion efficiency difficult. In addition, internal EGR and FAE exacerbate this issue leading temperature sensors located in the respective outflow ports measuring mixed out temperatures of hot and cold fluid streams.

In order to incorporate both effects a modified approach is proposed. In general, HPG and HPA ports are connected through the combustor, as shown in Figure 4(a), therefore mass flow rates through the respective ports (ignoring added fuel mass) will generally be equal in steady-state operation. Since loop flow ratio is generally greater than unity, the mass flow rate entering through the HPA port is then composed of both the fresh air supply $\dot{m}_{\rm LPA}$ and the internally circulated exhaust gas $\dot{m}_{\rm EGR}$. Thus, following the general flow pattern as illustrated in Figure 4 with internal EGR being present in the HPA port and neglecting FAE, flow leakage and the effect of rotational speed variation, the amount of EGR may be approximated as the difference in fresh air mass entering through the LPA port and the air/gas mixture mass exiting the wave rotor through the HPA port. Thus the amount of EGR becomes solely a function of loop flow ratio λ as described in Equation 2.

$$\dot{m}_{\rm EGR} = \dot{m}_{\rm HPA} - \dot{m}_{\rm LPA}$$

$$\psi_{\rm EGR} = \frac{\dot{m}_{\rm HPA} - \dot{m}_{\rm LPA}}{\dot{m}_{\rm HPA}} = \frac{\lambda - 1}{\lambda}$$
(2)

Using Equation 2 in combination with the mixed out temperature $T_{\mathrm{HPA},m}$ in the

HPA port and assuming the EGR temperature entering the HPA port is approximately the HPG inlet temperature $(T_{\text{HPA},h} \approx T_{\text{HPG}})$ one can determine the cold flow temperature $T_{\text{HPA},c}$ in the HPA port through mass averaging, as done in Equation 3.

$$T_{\text{HPA,c}} = \frac{\dot{m}_{\text{HPA}} T_{\text{HPA,m}} - \dot{m}_{\text{HPA}} T_{\text{HPA,h}}}{\dot{m}_{\text{LPA}}} \tag{3}$$

Thus, actual compression and expansion work can be formulated according to the first law of thermodynamics as

$$\dot{W}_c = \dot{m}_{LPA} c_{p,c} (T_{HPA,c} - T_{LPA}) + \dot{m}_{EGR} c_{p,h} (T_{HPA,h} - T_{LPG})$$

$$\dot{W}_x = \dot{m}_{LPG} c_{p,h} (T_{HPG} - T_{LPG}^{is})$$
(4)

Actual compression work in Equation 4 takes into account contribution from the compressed air stream and the recirculated EGR stream. Thus, one can formulate the equations for isentropic compression and expansion efficiency as the ratio of actual to isentropic work defined in Equation 4. Including an additional temperature difference to account for the change in temperature due to internal heat transfer across the two streams yields

$$\eta_{c} = \frac{\dot{m}_{LPA}c_{p,c}(T_{HPA}^{is} - T_{LPA}) + \dot{m}_{EGR}c_{p,h}(T_{HPA,h}^{is} - T_{LPG})}{\dot{m}_{LPA}c_{p,c}(T_{HPA,c} - T_{LPA} - \Delta T_{c}) + \dot{m}_{EGR}c_{p,h}(T_{HPA,h} - T_{LPG} - \Delta T_{c})}$$

$$\eta_{x} = \frac{\dot{m}_{LPG}c_{p,h}(T_{HPG} - T_{LPG} - \Delta T_{x})}{\dot{m}_{LPG}c_{p,h}(T_{HPG} - T_{LPG}^{is})} \tag{5}$$

where $c_{p,c}=1005 \mathrm{J/kg}$ -K and $c_{p,h}=1160 \mathrm{J/kg}$ -K refer to specific heats at constant pressure for cold and hot stream respectively, while \dot{m}_{LPA} and \dot{m}_{LPG} denote mass flow rates through the respective low pressure in- and outlet ports. The additional variables in Equation 5 introduced through ΔT_c and ΔT_e renders the system of equations underdetermined and thus not solvable. Only if one assumes that both temperature differences as well as both compression and expansion efficiency to be equal, that is $\Delta T_c = \Delta T_x$ and $\eta_c = \eta_x$, the system is left with one equation and one unknown and is thus solvable.

It should be noted that the resulting equation is an approximation and effects that cannot be captured with the proposed formulation, such as leakage flows and variations in rotational speed will impart an effect isentropic efficiency. The approach proposed by Wilson et al. [51] includes heat transfer but does not take fluid mixing into account, which results in significant underprediction of efficiencies. The method suggested in this study seeks to include both effects using reasonable approximations.

2.2. Bath μ -Wave Rotor Design

217

218

219

220

221

222

223

225

227

The rotor features a mean channel diameter of 60 mm, 46 channels with a maximum blade angle of 21.5° and completes three cycles per revolution. The geometric dimensions of the rotor and the corresponding port solution is shown in Figure 5 and a summary of the most important parameters including design operating conditions are given in Table 1.

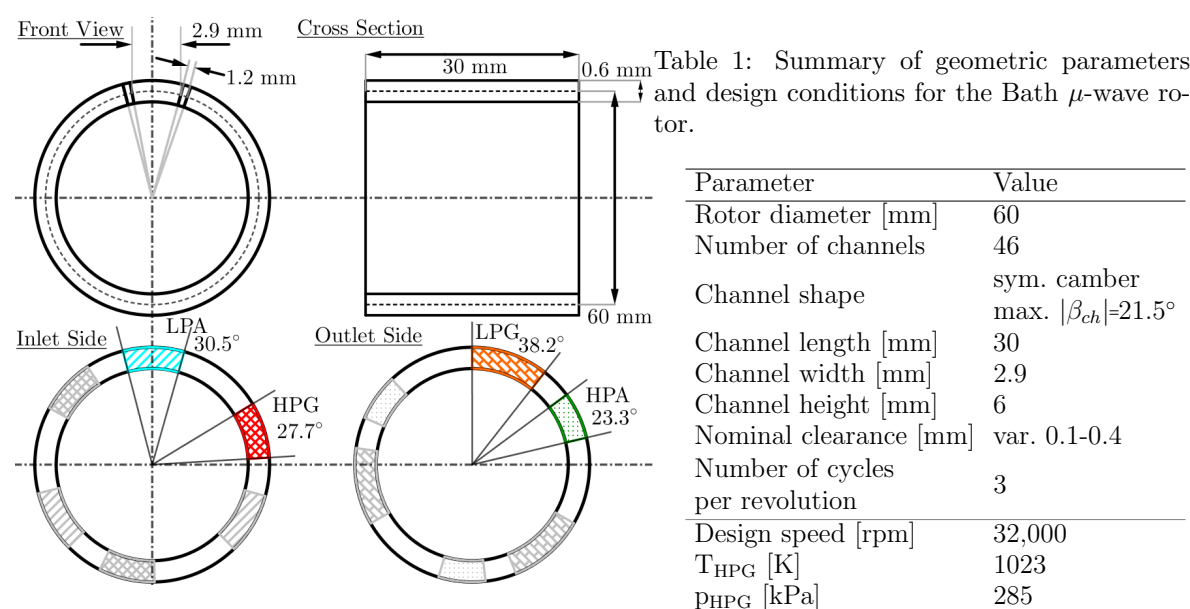


Figure 5: Schematic showin rotor dimensions as well as port solution.

Parameter	Value
Rotor diameter [mm]	60
Number of channels	46
Channel shane	sym. camber
Channel shape	max. $ \beta_{ch} = 21.5^{\circ}$
Channel length [mm]	30
Channel width [mm]	2.9
Channel height [mm]	6
Nominal clearance [mm]	var. 0.1-0.4
Number of cycles	3
per revolution	9
Design speed [rpm]	32,000
T_{HPG} [K]	1023
p _{HPG} [kPa]	285
p _{LPG} [kPa]	103

To facilitate comparison among different wave rotor designs Wilson and Fronek [36] and Nagashima et al. [3] defined non-dimensional parameters for finite passage opening T, viscosity F and leakage flow G. These are given as

$$T = \frac{wa}{UL}, \ F = \frac{\sqrt{\nu L/a}}{D_h}, \ G = \frac{2\delta}{h}$$
 (6)

Table 2 lists a comparison of these non-dimensional performance parameters for various realised wave rotors. This allows direct comparison and although this is somewhat difficult to do for pure pressure exchangers operating at low temperatures and wave rotor turbines operating at high temperatures, one can see that the Bath μ -wave rotor performs similarly with respect to finite opening timing effects despite a relatively short rotor length. As expected, due to the small size compared with larger designs viscous losses become more pronounced and is similar to the micro wave rotor study conducted at USAF [40]. Nonetheless, the by far most significant loss mechanism for the wave rotor turbine is leakage between both stators and the rotor. At the design clearance of 0.1 mm this is at best similar to the ABB Comprex and the two USAF designs. However, as alluded to in the next section, it is expected that this parameter is significantly higher during experimental testing as a consequence of uneven thermal expansion of stators and the shaft-rotor assembly. Therefore, the G-parameter will most likely range between values of approximately 0.2-0.23.

Table 2: Comparison of realised wave rotors with the University of Bath (UoB) μ -wave rotor turbine (amended from [3]).

	Kentfield 3-port PE [34]	NASA 3-port PE [36]	USAF[19] PWS 4-port TF	USAF[40] PWS 4-port TF	ABB [52] Comprex 4-port RF	Pearson [5] 6-port TF wave engine	UoB 4-port TF μ -wave turbine
Т	0.39^{\dagger}	0.082^{\dagger}	0.29^{\dagger}	0.21^{\dagger}	0.467	0.3^{\dagger}	0.37 [†]
F	0.0046^{\dagger}	0.017^{\dagger}	0.0082^{\dagger}	0.0121^\dagger	0.0067	n.a.	0.013^{\dagger}
G	0.0064	0.025-0.075	0.032	0.038	0.030	n.a.	0.033-0.132

^{† -} based on atmospheric values

Figure 6(a) shows an exploded view of the wave rotor unit in CAD. It exhibits the wave rotor itself with its 46 curved channels along with an outer sleeve that is manufactured separately and subsequently installed with an interference fit on to the wave rotor by shrink-fitting. Additionally, inlet and outlet stator with the respective openings that trigger shock and expansion waves are highlighted as well. They feature appropriate flanges and clamps to connect the stator pipes to the manifolds. A central housing connects the two stators. Towards the inlet side, the centre bolt with shaft that connects the wave rotor with the dynamometer is shown as well. The connection of dynamometer and wave rotor unit is done through a two-plane coupling. Reference surfaces on the dynamometer side and the wave rotor mounting bracket ensure proper alignment of both units. The bearing housing contains the two roller bearings (and bearing preload spacer) separated by a spacer. Provisions for cooling channels between inner and outer bearing housing are made to ensure a controlled thermal management of the sealed-for-life bearings.

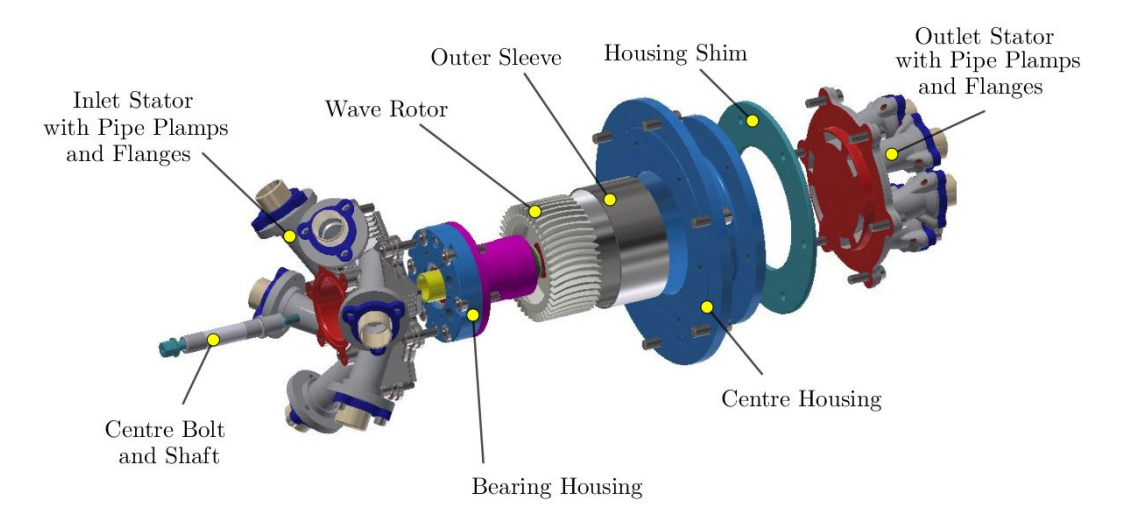


Figure 6: Exploded view of the wave rotor assembly.

The final manufactured parts are shown in Figure 7. Both stators were produced from Inconel 625 using selective laser melting (SLM) additive manufacturing technique and machined to their final finish. This can be seen in Figure 7(a). The rotor, its sleeve and the centre casing were machined from solid, after which rotor and outer sleeve were mated to give the final shrouded version, as given in Figure 7(b). Figure 8(a) depicts the assembled wave rotor device including in- and outlet manifolds that distribute the flow to the respective port. In addition, the hose couplings for the cooling circuit of the bearing housing as well as the single-plane coupling that connects the wave rotor device to the dynamometer are shown in Figure 8(b).

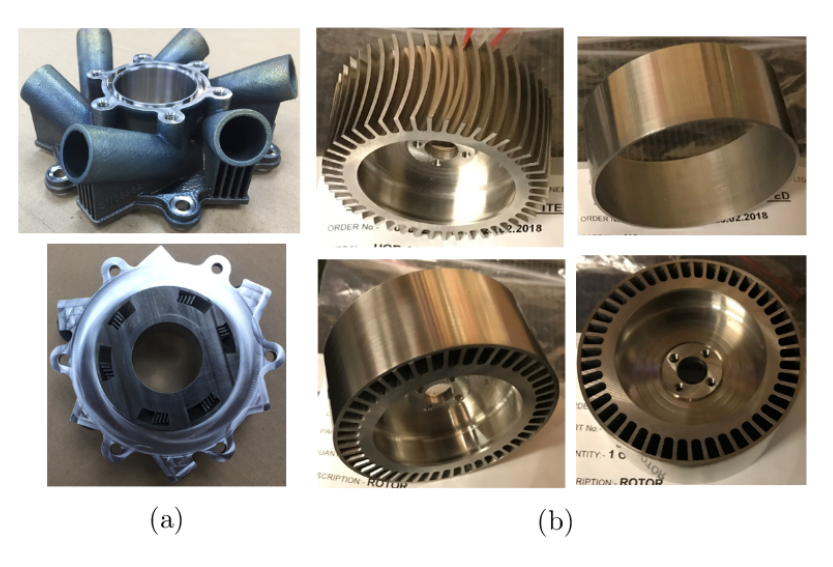


Figure 7: Manufactured parts: (a) inlet on top and outlet stator on the bottom. (b) Rotor showing channel curvature and its outer sleeve.

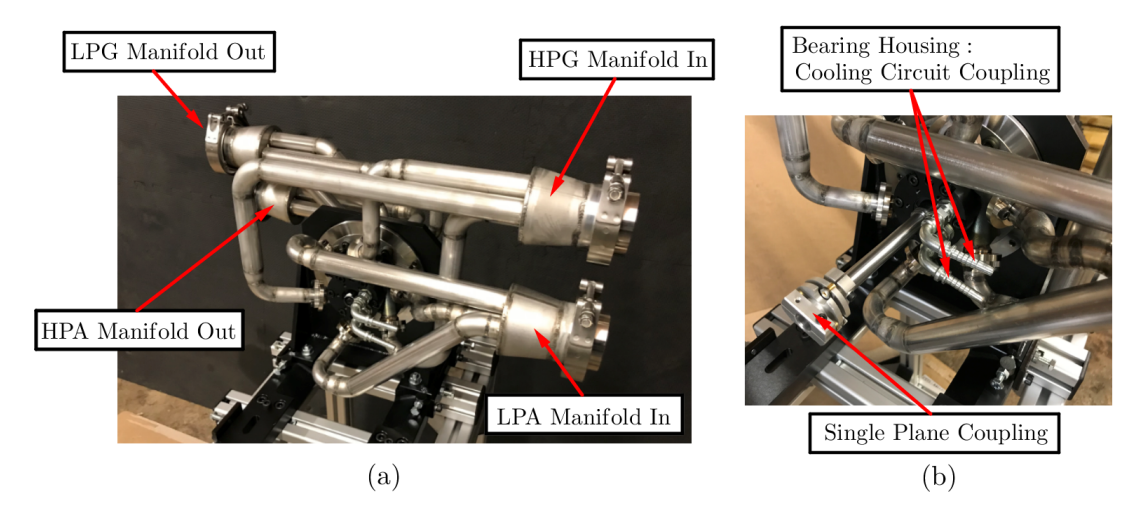


Figure 8: (a) Assembled wave rotor machine with in- and outlet manifolds. (b) Couplings for bearing housing water cooling circuit and single-plane coupling to link wave rotor with load cell.

2.3. Experimental Setup

267

268

269

270

2.3.1. Gas Stand Layout and Instrumentation

For the characterisation of the wave rotor, laboratory experiments were performed on the University of Bath turbocharger gas stand. The setup allows to perform variation of operating conditions, such as dynamometer excitation load, loop flow ratio λ , mass flow rates and inlet pressures in the high- and low pressure inflow ducts,

as well as the backpressure through both high- and low pressure outflow ducts. In this scenario, one can measure both generated power and generated pressure ratio, as well as the corresponding port outlet temperatures.

273

274

275

276

277

278

279

280

281

282

283

284

285

286

287

288

289

290

291

292

293

294

295

296

297

298

299

300

301

302

303

304

305

306

307

308

The wave rotor gas stand, as depicted in the schematic of Figure 9, consists of an open-loop configuration and is able to provide a maximum source pressure of 7 bar absolute generated from a set of external rotary type compressors. Moisture in the delivered air stream is removed via a refrigerated and compressed air drier conditioning the incoming dry air to approximately 15°C. The incoming air pressure can be regulated via a regulator valve (element 2 in Figure 9). Pressure and mass flow rates delivered on both high and low pressure legs are controlled via an actuated ball valve and two pneumatically controlled 2" variable orifice control valves (elements 4) located on each of the high and low pressure pipework legs. The high pressure leg further features a differential pressure V-cone mass flow meter (element 5) with a flow range from 0.015 kg/s to 0.15 kg/s and a Bowman air-to-air heat exchanger (element 6) that preheats the incoming (cold) air using the hot exhaust gas that would normally be expelled without being used. Downstream of the heat exchanger sits an Axis Design electric heater (element 7), able of providing up to 44 kW to the flowing air stream, resulting in a maximum deliverable temperature of around 750°C. It is noteworthy that pipework between the electric heater and the wave rotor is fully insulated in order to minimise heat losses between rotor and the heater outlet. On the low pressure leg the incoming air is directed through another differential pressure V-cone mass flow meter (element 8) with a mass flow range from 0.005kg/s-0.05kg/s before reaching the wave rotor inlet manifold.

Both wave rotor bearing housing and eddy-current dynamometer have dedicated cooling circuits (elements 16 and 17 respectively) that should ensure smooth and continuous operation. Cooling water is fed via the main water valve from the university pond and filtered before running through the respective cooling circuits. A pressure sensor upstream of the dynamometer cooling circuit ensures the maximum allowable pressure of 1.9 barA at the inlet of the dynamometer cooling pipes is not exceeded during testing. In addition, a flow meter was installed on the cooling circuit of the bearing housing ensuring a water flow rate of approximately 2 L/min.

On the high and low pressure outflow legs two pneumatically actuated variable orifice control valves (elements 11 and 14 respectively) control the backpressure experienced by the wave rotor. In this scenario the gate valve on the HPA leg provides the means to match the mass flow rates in the high pressure zone HPG-HPA. This requires the computation of the mass flow rate through the HPA leg, which is achieved through a 2" differential pressure V-cone mass flow meter (element 13) with a rated flow range from 0.015 kg/s to 0.15 kg/s. Due to temperature limitations of the mass

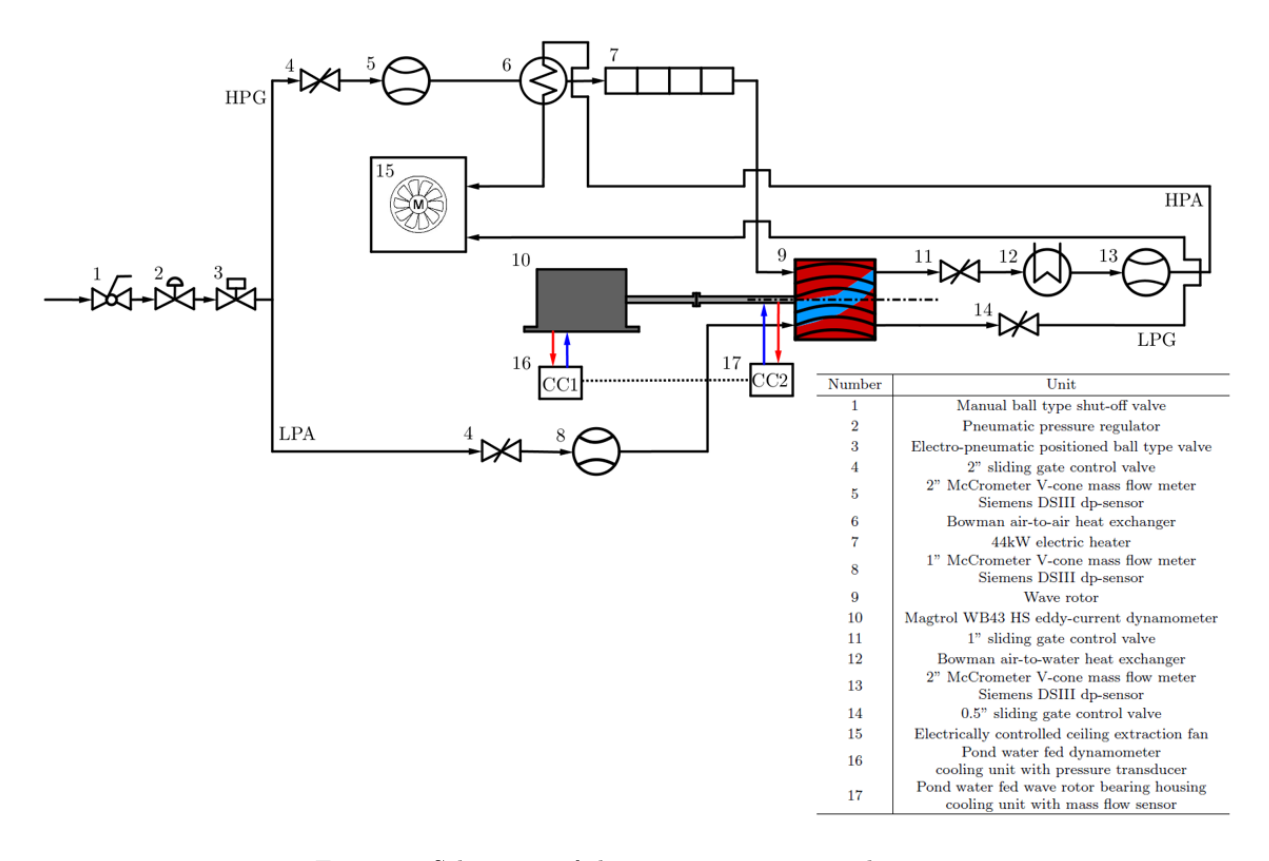


Figure 9: Schematic of the wave rotor gas stand test setup.

flow meter instrumentation, in particular the PT100 sensor necessary for air density calculation, a Bowman air-to-water heat exchanger is located upstream of the mass flow meter in order to reduce the hot exhaust gas temperature down to approximately 30°C.

Wave rotor performance data are gathered by means of the sensors listed in Table 3.

The list gives an account of all the sensors used throughout the campaign including their measurement range and accuracy. In order to quantify the combined uncertainty of all measured data, the British Standard [53] is used, assuming a rectangular distribution and thus equal probability for all values. This encompasses pressure transducers and thermocouples located just upstream of the intake manifolds and downstream of the outflow manifolds. Mass flow rates are determined through differential pressure sensors and Bernoulli's theorem for the conservation of energy along a streamline. PRT temperature sensors and pressure transducers located on the high pressure side of the v-cone allow calculation of flow density and together with the

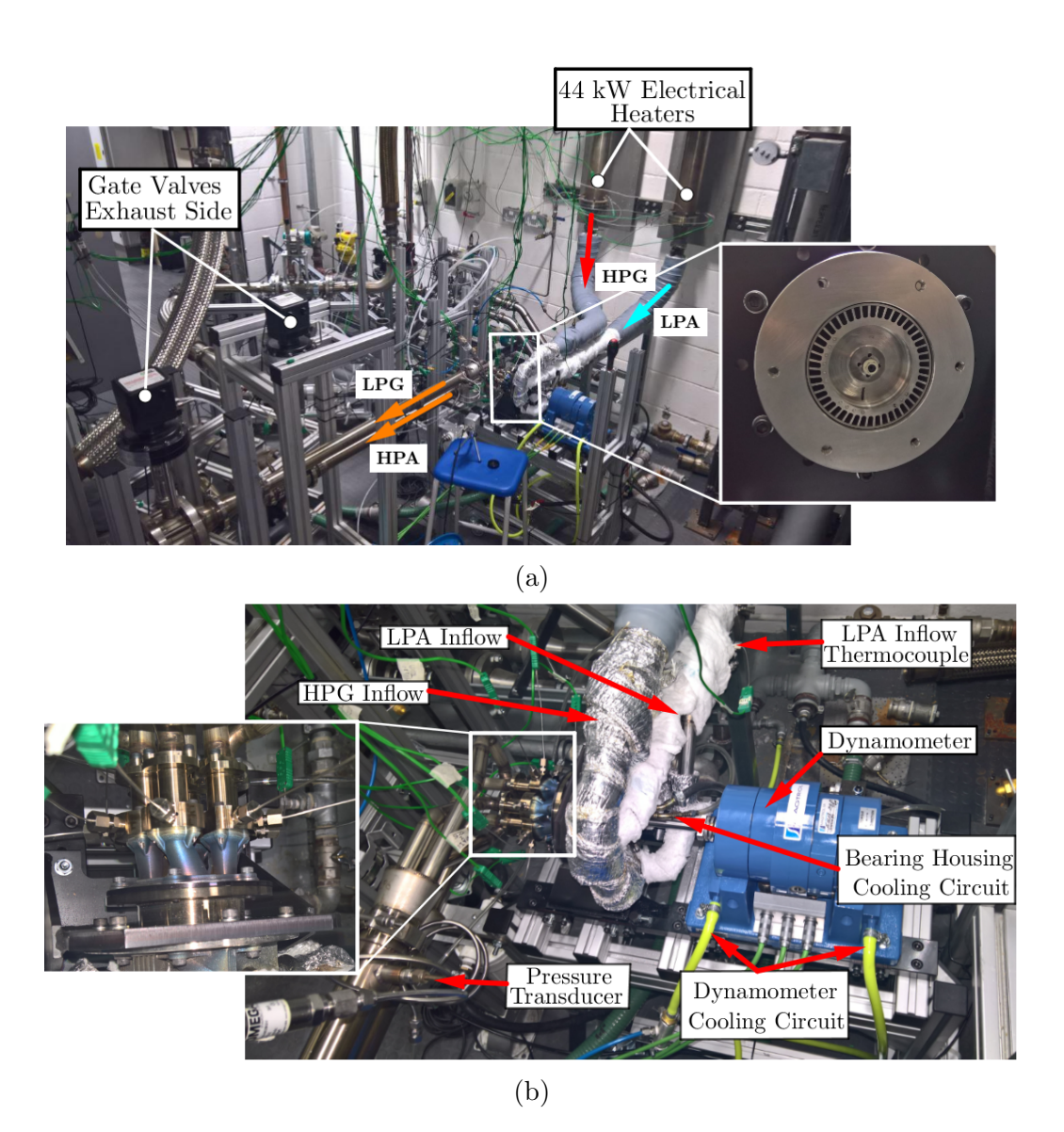


Figure 10: (a) Photograph as taken from the gas stand showing experimental setup. In particular, the electrical heaters upstream of the wave rotor machine can be seen. It is important to note that merely the HPG heater is in use throughout this study. Furthermore, the wave rotor within the centre housing as well as the downstream gate valves are highlighted. (b) Photograph showing wave rotor gas stand including coupling to the dynamometer, cooling circuits to dynamometer and bearing housing, insulated inflow ducts with instrumentation (thermocouple shown, pressure transducer not visible), instrumented outflow ducts as well as thermocouple arrangement close to the rotor outlet.

Table 3: List of sensors used throughout testing including their measurement range and their accuracy as stated by their manufacturers. It is noteworthy that response times and sampling frequency are not reported as the sensors measure steady state data.

Sensor	Range	Nominal Accuracy
1.5 mm K-type thermocouple	-200°C - 1260°C	±0.0075T from 333°C to 1200°C ±2.5°C from -40°C to 333°C
PRT	-50°C - 200°C	$\pm 0.3 + 0.005T$
V-cone mass flow meter	0.015 kg/s - 0.015kg/s (HPG, HPA) 0.005 kg/s - 0.05kg/s (LPA)	$\pm 0.5\%$
Static pressure	0 barG - 7 barG (HPG, HPA) 0 barG - 2 barG (LPG) 0 barA - 3.5 barA (LPA)	0.08%
Differential pressure	0 bar-0.06 bar (HPG, HPA) 0 bar - 0.0049768 bar (LPA)	$\pm 0.5\%$
Rotor Torque	0-1.5 Nm	$\pm 0.3\% FS$
Rotor Speed	0-65,000 rpm	$\pm 0.1\% FS$

differential pressure yield flow velocity. Using mass flow rates in conjunction with the static temperature and pressure probes one can determine total port properties through the first law of thermodynamics, as done in Equation 1.

$$p_t = p_s \left(1 + \frac{(\gamma - 1)}{2} \frac{\dot{m}^2 T_s R}{p_s^2 \gamma A^2} \right)^{\gamma/(\gamma - 1)} \tag{7}$$

28 Total-to-total pressure ratio is thus defined as

$$\Pi_c = \frac{p_{t,HPA}}{p_{t,LPA}} \tag{8}$$

In addition to the manifold in- and outflow conditions additional measurement sections with a set of thermocouples was installed around two rotor lengths downstream of the rotor-outlet stator interface, as shown in Figure 10. This should allow measurement of the outflow temperatures from HPA and LPG ports and give a notion of the temperature distribution and the behaviour of internal exhaust gas recirculation (EGR) in the HPA duct by making use of periodicity and placing the thermocouples ends at various positions within the duct as indicated in Figure 11(a), which combined give the measurement points shown in Figure 11(b). Each thermocouple position is assigned a number and it is important to notice that thermocouples 1 and 3 are positioned towards the outer diameter, while 2 and 4 towards the centre. Due to the limited amount of space within the 15mm duct only six probes could

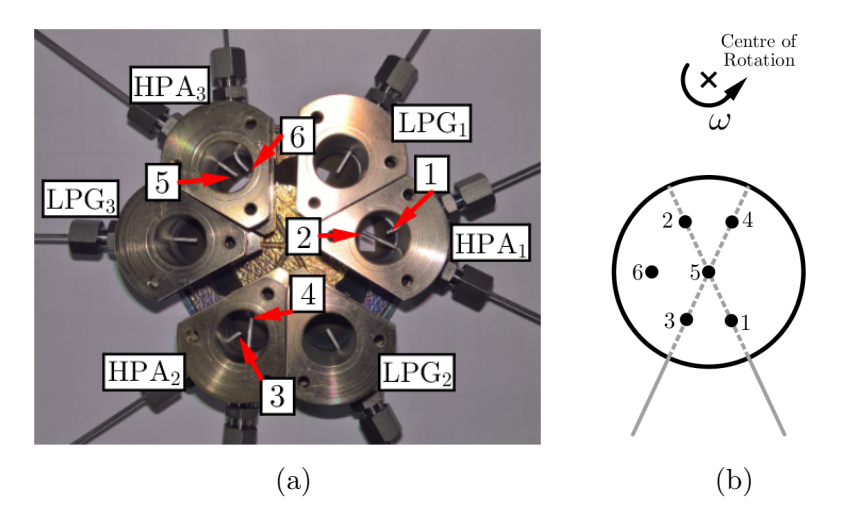


Figure 11: (a) measurement sections for thermocouple installation just downstream of the outlet stator. Each LPG measurement section features a single temperature probe located in the centre of each duct. For the HPA duct the temperature probes were arranged at different positions resulting in the distribution shown in (b).

be fitted across all three HPA ducts. In addition, limited accessibility of the stator ports required to place the measurement section relatively far downstream of the rotor outlets, increasing the risk of thermal diffusion smearing the cold/hot gas interface. 343

2.3.2. Experimental Campaign

340

341

342

344

345

346

347

349

350

351

352

353

354

355

356

357

358

The laboratory experiments seek to investigate the behaviour of the designed wave rotor turbine and the sensitivity of outlet temperatures, total-to-total pressure ratio (defined in Equation 8) and power output as rotational speed, loop flow ratio λ (as given in Equation 1) and inlet temperatures are varied. Table 4 summarises all test conditions. Firstly, loop flow sweeps from 1.7 to 3.2 in increments of 0.5 are performed at 500°C. In addition rotational speed is swept in steps of 2,000 rpm from 22,000 rpm to the design speed of 32,000 rpm. This is repeated for increased inlet temperature of 600°C, albeit solely at loop flow ratio 1.7.

In addition, the effect of increased axial leakage gap is identified, too. Initial test for λ and rotational speed sweeps are carried out at a nominal leakage gap of 0.2/0.25 mm. Experiments at elevated inlet temperature of 600°C are then performed at both 0.2/0.25 mm and 0.3/0.3 mm nominal leakage gap in an effort to investigate the effect of increased leakage on the dependant variables. It is noteworthy that the baseline model was designed for an axial clearance of 0.1 mm at both in- and outlet. However, during experimental testing it soon transpired the target clearance was difficult to

Table 4: Test conditions for the initial wave rotor turbine laboratory experiments.

Inlet Temperature T in °C	Loop Flow Ratio	Rotational Speed in rpm	Nominal Leakage Gap in mm
500	(1.7/2.2/2.7/3.2)		0.2/0.25
600	1.7	22,000-32,000	0.2/0.25 $0.3/0.3$

achieve as a result of uneven thermal expansion between the rotor assembly and both in- and outlet stator. The compact size of the rotor in combination with the pressurised and thermally elevated environment prevailing within the stator housings preclude the application of a standard gap measurement sensor. Therefore, it was not possible to determine the actual leakage gap when all machinery was running in thermal equilibrium and throughout this study nominal clearances are given only.

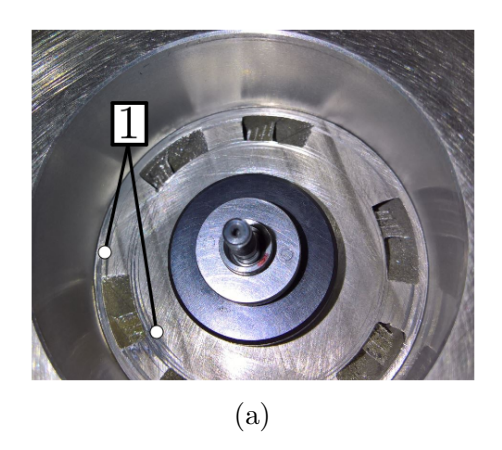
The start-up procedure followed the following routine: Initially, all outlet valves are completely opened, the heater turned and brake both turned off. Then, the flow through the HPG duct is gradually increased by opening the corresponding gate valve. As soon as the rotor starts spinning, the brake excitation is increased maintaining a rotational speed of around 15,000 rpm. After that, the LPA inlet valve is opened as well and the brake excitation adjusted accordingly to maintain rotational speed. In the process, both inlet valves are then alternatively opened such that the loop flow ratio stays within a range of 1.7-2.0 until the maximum mass flow rate reaches approximately 35-40 g/s. As soon as this condition is reached the heater demand temperature is set to 100° C. When this is reached and the thermal camera indicates an approximate thermally stable condition, the temperature is increased in 50° C steps up to the desired testing temperature.

3. Results and Discussion

3.1. Experimental Results

3.1.1. Limitations and Issues

Initial tests commenced with a nominal (cold) clearance of 0.1 mm on both in- and outlet. It was found that when the inlet temperature is increased in short intervals, the rotor - being housed in a closed volume - heats up quicker than the thermally more inert and to ambient conditions exposed housing components. This resulted in thermal expansion of the rotor towards the inlet side resulting in contact with the inlet stator face. The incurred damage was not catastrophic and resulted in minor scratches to rotor and stator, as shown in Figure 12. As a result, the temperature increments were reduced to the aforementioned 50°C and sufficient time allowed for all components to thermally expand sufficiently. Furthermore, it was decided to start testing with rather conservative clearances of 0.2 mm/0.25 mm and 0.3 mm/0.3 mm at in- and outlet respectively.



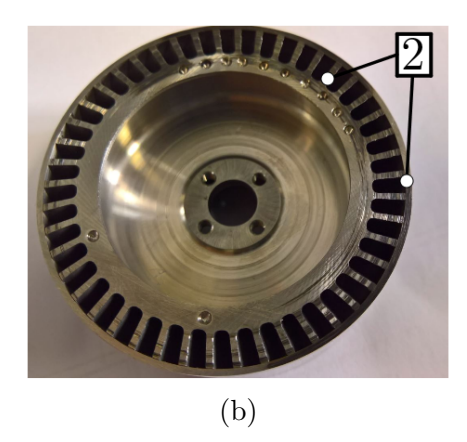


Figure 12: Minor damage to rotor and stator as a result of quick temperature increase and transiently imbalanced expansion between rotor and stator.

Extended exposure to elevated temperatures proved problematic with respect to bearing service life, despite the water-cooled bearing housing. It transpired that exposing the machine to around 600° C for around an hour results in all the lubrication from the bearings to be completely evaporated despite the cooled bearing housing. Interestingly, the bearing seals and cages were not destroyed showing no signs of discolouration through heat exposure. This may indicate that the anticipated heat conduction through the shaft is less problematic than anticipated and that the air temperature reaching the bearing closest to the rotor suffices to evaporate the lubricant completely.

3.1.2. Loop Flow Ratio and Rotational Speed Variation

The results shown in Figure 13 illustrate wave rotor performance data as a function of loop flow ratio and wave rotor speed done at 500°C HPG inlet temperature and a nominal clearance of 0.20 mm on the inlet and 0.25 mm on the outlet side. In particular, the graphs shown in Figure 13(a) depict total-to-total pressure ratio, relative difference between HPG and HPA total pressures, LPA inlet pressure, while Figure 13(b) displays shaft power output and averaged HPA and LPG outlet temperature respectively.

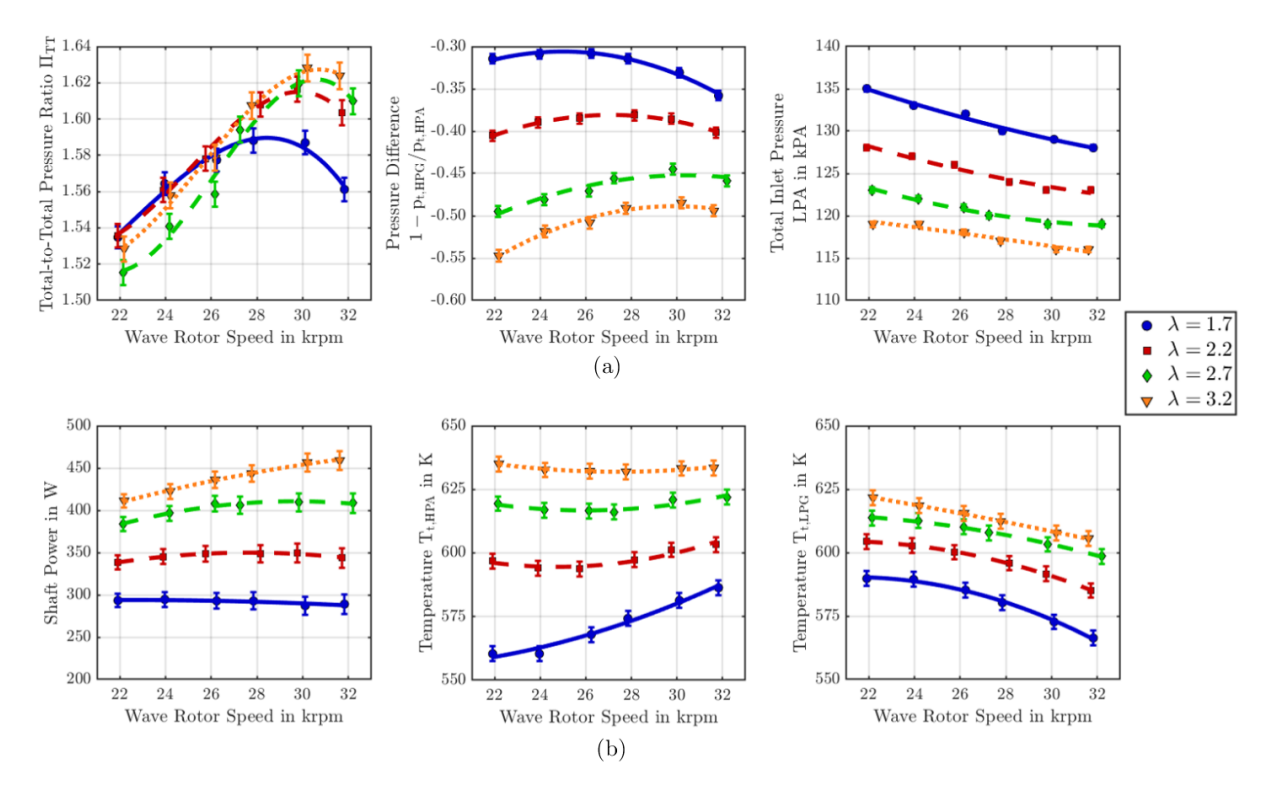


Figure 13: Wave rotor performance data for variations in loop flow ratio and rotational speed at 500°C HPG inlet temperature and a nominal clearance of 0.20 mm on inlet and 0.25 mm on outlet side. (a) Wave rotor data of total-to-total pressure ratio (left), relative pressure difference in the combustor loop between HPG and HPA (centre) as well as the total inlet pressure in the LPA inlet. (b) gives shaft power output (left) and demonstrates averaged total temperature at HPA and LPG (centre and left respectively).

Pressure ratio variations with speed follows a parabolic distribution with speed across all loop flow ratios. Variations are, however, rather subtle, implying relatively small sensitivity to changes in loop flow ratio and rotational speed. Nonetheless, there seems to be an increase in the achieved pressure ratio for higher λ ratios and

there appears to be a drift of the peak towards higher rotational speeds with greater λ ratios.

As the tests were conducted at relatively large leakage gaps (in particular at the outlet side) and lower total inlet temperature, the recorded relatively difference across the combustor is rather large and would necessitate (an unrealistically strong) pressure gain combustor linked in between. Nonetheless, it becomes apparent that lower loop flow ratios result in smaller required 'pressure gain'. In addition, while the peak in relative error tends to be more towards higher rotational speeds, it appears to shift towards lower rotational speeds with decreasing loop flow ratio.

Higher loop flow ratios signify lower LPA inlet pressures, as seen in the right hand side graph of Figure 13(a). This signifies lower average pressure prevailing within the passages and thus lower resistance as the channel is exposed to the HPG port leading to higher mass flow rates and greater power extraction.

Variation in rotational speed yields relatively small changes in wave rotor power with an increasing gradient towards lower rotational speeds when λ ratios are increased, as illustrated in the left hand graph of Figure 13(b). The reason for witnessing an absolute increase in power output for higher loop flow ratios is founded on the fact that the results as shown where generated for constant inlet pressures resulting in variations in inlet mass flow rates through the HPG inlet.

Examining the outlet temperature distribution for HPA and LPG illustrated in the bottom centre and right graphs of Figure 13(b) shows that an increase in loop flow ratio results in both an increase of HPA and LPG outlet temperature, which is to be expected as higher loop flow ratios indicate less cold air being fed to the rotor. Therefore, at constant inlet temperature loop flow ratios converging towards unity contribute lower outlet port temperatures, lower internal EGR rates. In addition, one should remember that the expanded and compressed stream act are in thermal contact with each other within the channels and basically act as an internal recuperator, where the hot exhaust gases heat up the incoming fresh air. From the data it transpires that there occurs FAE close to the design speed at 32,000 rpm. This manifests itself in a lower LPG temperature and higher HPA temperature. As speed is reduced, FAE is gradually diminished, which accounts for a reduced amount of EGR in the HPA port. Therefore, mixed-out temperatures in the HPA port decline with decreasing rotor speed. Conversely, LPG port temperatures increase as FAE decreases through lower wave rotor speed. The data thus show that, in order to minimise FAE and EGR it is desireable to operating towards the lower end of the speed range, while for pressure ratio and combustor loop pressure difference, one would want to operate closer towards the design speed.

A detailed investigation of the outlet temperature distribution is provided by

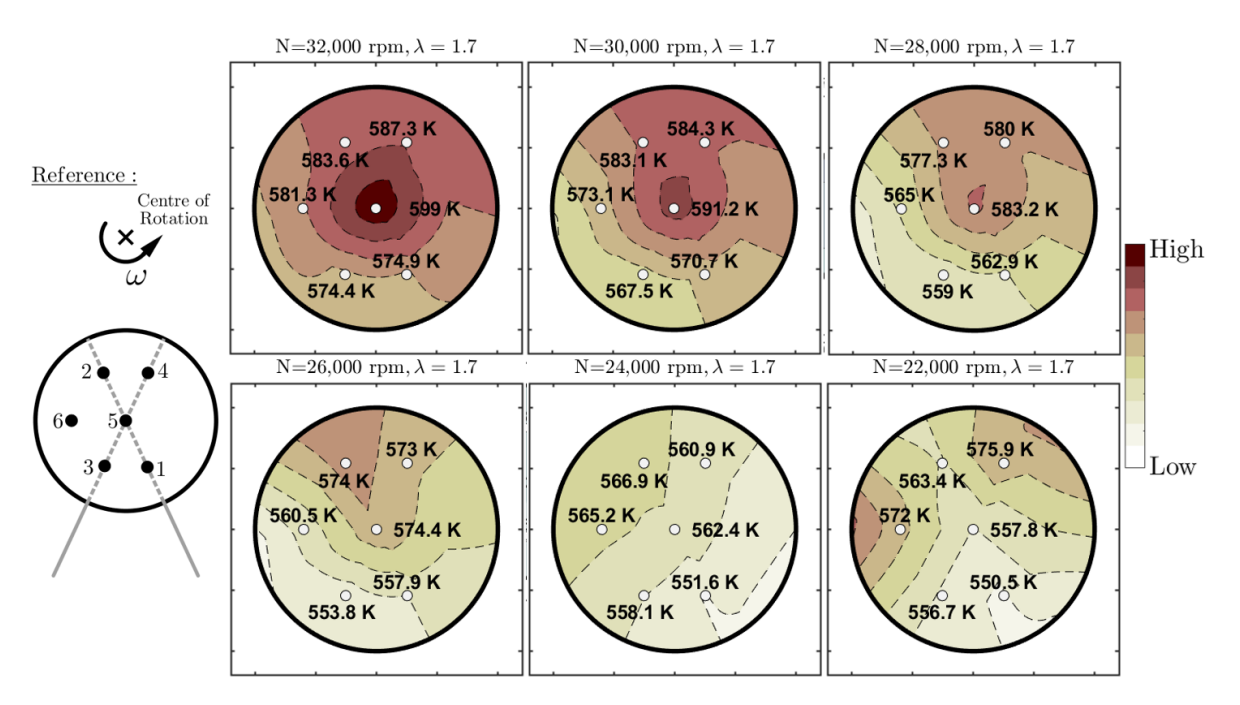


Figure 14: Contour plot showing temperature distribution in the measurement section downstream of the HPA port. Data outlines the both the effects of rotational speed variation and centrifugal forces on the HPA temperature distribution for a constant loop flow ratio of 1.7.

the contour plots in Figure 14. All data were gathered for a λ ratio of 1.7 and gives further details on the interaction of cold and hot streams as well as exhaust gas recirculation. The temperature differences are relatively small, which is in part a result of diffusion and flow mixing taking place between the hot and cold fluid streams. Nonetheless, significant information from the data can be extracted and inferences regarding the characteristics made. The temperature probes reveal that-as one might expect- the colder stream appears to be moved towards the outer shroud of the wave rotor as a consequence of the centrifugal forces, which manifests itself in slightly lower temperatures towards probes 1 and 3. This trend is shown throughout all rotational speeds. The reduction in FAE in the LPG port and EGR in the HPA ducts with decreasing rotor speed is also reflected in the contour plots resulting in lower detected minimum temperature that increases from around 550 K for 22,000 rpm to 575 K at the design speed of 32,000 rpm.

The effect of varying loop flow ratio on the HPA temperature distribution can be witnessed in Figure 15. The location of the cold stream appears to remain relatively unchanged with centrifugal forces still accounting for pushing it outwards. Nonetheless, one can see that increased EGR rate accounts for considerably larger HPA outlet

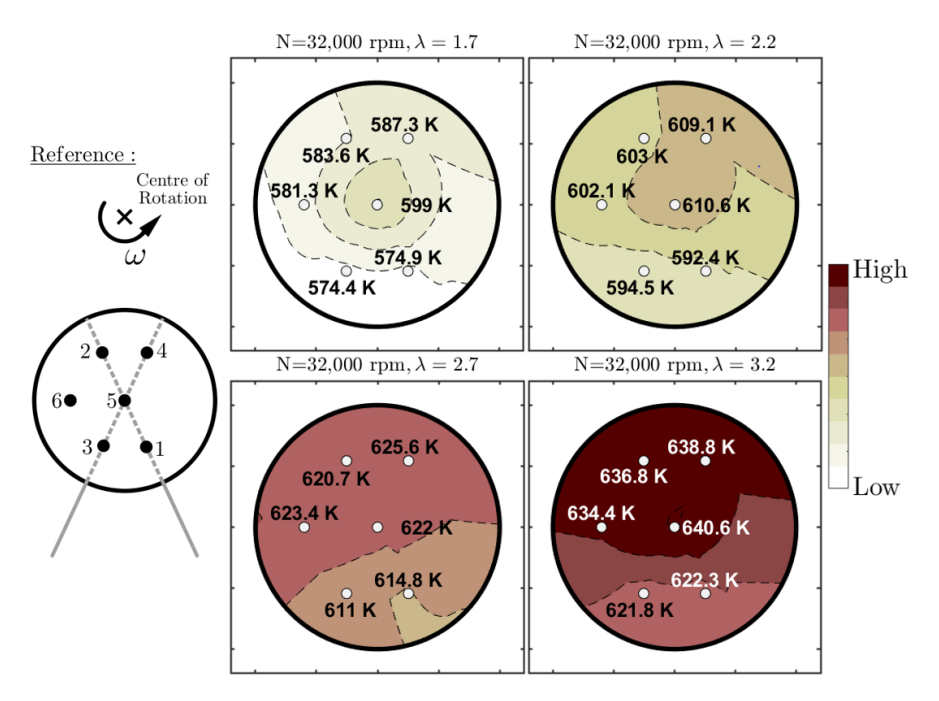


Figure 15: Contour plots created with data collected in the measurement sections downstream of the HPA port exhibiting the effect of loop flow variation on the high pressure exhaust temperature distribution.

temperatures with the maximum increasing from 576 K at $\lambda=1.7$ to 641 K at $\lambda=3.2$. Based on temperature alone, higher inlet temperature signifies less temperature rise demanded from the combustor; however, higher EGR rates signify less oxygen in the delivered air/gas mixture and thus potential ramifications regarding flame stability.

Using the efficiency equation introduced in Equation 5 results in the estimated compression/expansion efficiency distribution given in Figure 16. The maximum efficiency is witnessed for $\lambda=3.2$ and is at around 80%. Interestingly, efficiency appears to decrease as one approaches a loop flow ratio of unity, which is in part a result of a more distinct effect of FAE that becomes more pronounced the closer the wave rotor operates to its design speed of 32,000 rpm and the lower the loop flow ratio λ (as seen in the bottom right plot of Figure 13). Although the effects of FAE are not directly incorporated into the efficiency formula, it is implicitly accounted for through the mixed out temperatures in the LPG port used for the calculation of isentropic expansion ratio. For higher loop flow ratios the cold air stream is generally narrower and EGR rates at a higher level leaving variations in rotational speed with less of an effect on efficiency and also lower variations for loop flow ratios of 2.2 and higher.

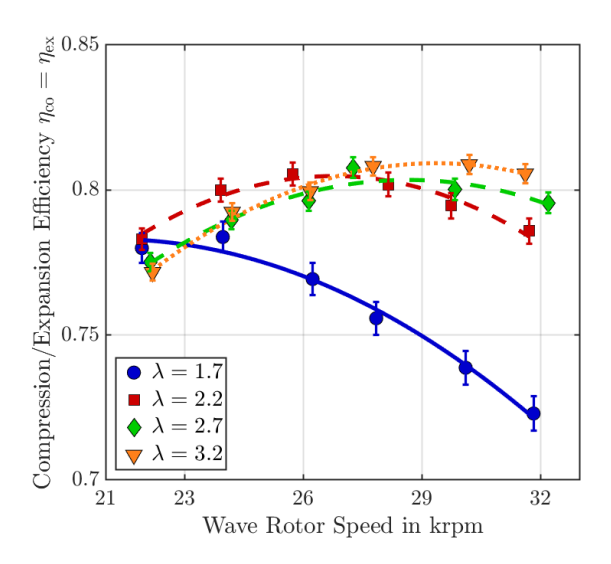


Figure 16: Variation in compression/expansion efficiency with loop flow ratio and rotational speed.

3.1.3. Axial Leakage Variation

Laboratory results concerning the impact of increased axial leakage on wave rotor performance are demonstrated in Figure 17(a) and (b). Data were collected for two different nominal leakage gaps of 0.2/0.25 mm and 0.3/0.3 mm respectively, for constant HPG inlet temperature of 500°C and constant HPG inlet pressure of approximately 275 kPA and a constant loop flow ratio of 1.7.

In the top left plot, a pronounced effect of increased leakage on the produced pressure ratio can be witnessed. In detail, the achieved pressure ratio undergoes a reduction of approximately 15%. The reason for this lies predominantly in a more pronounced interaction between neighbouring rotor channels and a significant reduction in the reflected, secondary pressure wave. As lower leakage yields higher pressure ratio and thus enhanced energy transfer it is logical that the relative difference across the combustor loop is reduced and less 'pressure gain' necessary, as disclosed in the top right chart of Figure 17(a).

Interestingly, for reduced axial leakage, shaft power output appears to be reduced. One would expect a rather similar level of power output, in particular as boundary conditions regarding inlet pressures and mass flow rates are of similar degree. The reason for the shown difference most likely lies in the fact that soon after testing of the low leakage case, a bearing failure was detected. It is thus likely that the bearings exerted a larger parasitic drag and thus a reduction in measured torque for the low leakage experiments. For high leakage tests a fresh set of bearings was installed, resulting in a larger reported power output.

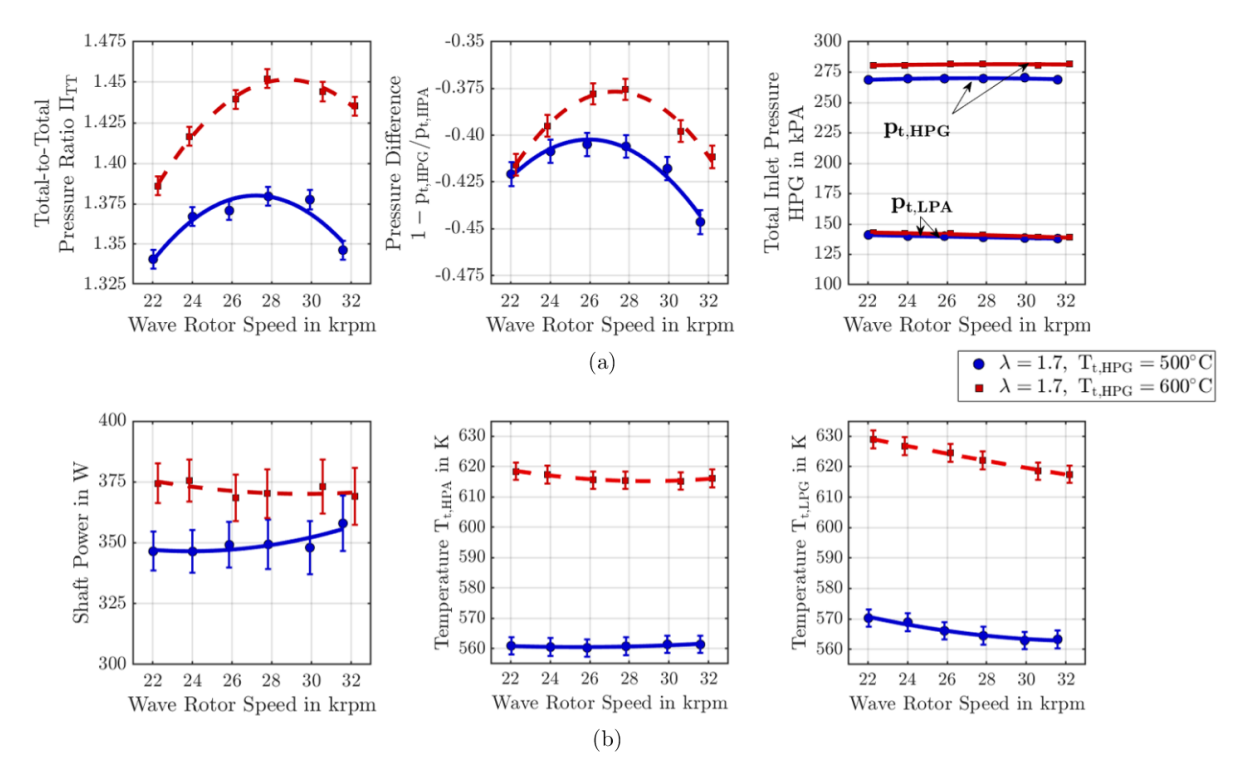


Figure 17: Wave rotor performance data for variations in nominal leakage clearance and rotational speed at 500°C HPG inlet temperature. (a) gives total-to-total pressure ratio (left), relative pressure difference in the combustor loop between HPG and HPA (centre) as well as the total inlet pressure in the HPG and LPA inlet (right). (b) displays shaft power output (left) and averaged total temperature at HPA (centre) and LPG (right).

Reduced axial leakage fosters less interaction among rotor passages and with the leakage cavity. As a consequence, one can clearly distinguish between the effect of FAE and EGR in both HPA and LPG averaged outlet temperatures as shown in Figure 17(b). As laid out previously, there is some amount of FAE and a maximum amount of EGR close to the design speed at 32,000 rpm. This is gradually reduced when the rotor spins at lower speeds. However, at larger leakage gaps this effect is greatly attenuated and outlet temperature becomes less sensitive to changes in rotor speed. A possible contributor to this reduced sensitivity may stem from the previously noted interaction among channels and hence, greater diffusion and mixing taking place within the channel allowing for instance more hot air ingestion into the channel as it passes by the LPA port and before it is even exposed to the hot conditions in the HPG port.

The effect of increased axial clearance gaps on compression/expansion efficiency

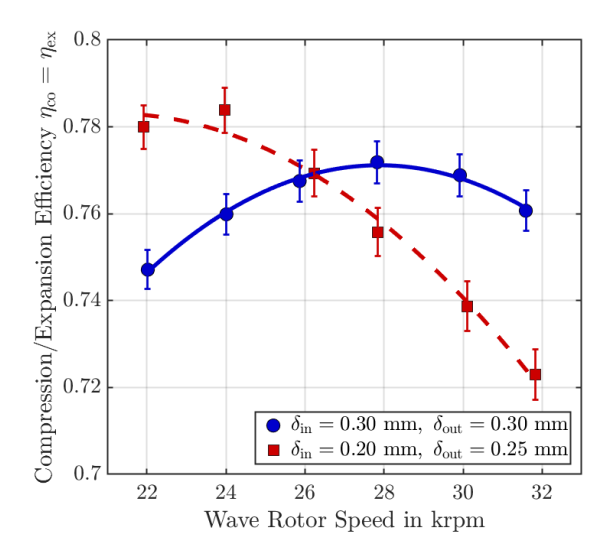


Figure 18: Variation in compression/expansion efficiency with loop flow ratio and rotational speed for two different nominal leakage gaps at constant peak inlet temperature.

for a loop flow ratio of 1.7 and a peak inlet temperature of 500°C is shown in Figure 18. At lower clearance the effect of FAE is more pronounced leading to a drop in efficiency as one approaches higher rotational speeds. As already seen in Figure 16 and in combination with the mixed out temperatures given in Figure 17 increased leakage gap lead to less sensitive efficiency distributions with respect to rotational speed. The increased leakage gap acts in a similar way to a higher loop flow ratio in that respect.

3.1.4. Inlet Temperature Variation

The final comparison conducted deals with the effect of HPA inlet temperature variation from 500°C to 600°C with rotational speed and constant HPG inlet pressure of approximately 275 kPA and a constant loop flow ratio of 1.7. All data were collected using a nominal leakage gap of 0.3/0.3 mm and is displayed in Figure 19.

An increase in inlet temperature at constant inlet boundary conditions (inlet pressure and mass flow rate) represents an increase in enthalpy and thus more energy being transferred to the rotor. As a result more energy can be transferred between hot and cold stream through wave action and more power extracted through momentum change. This is exemplified in the pressure ratio and power output graphs given in Figure 17(a) and (b). At constant LPA inlet pressure this increase in energy transfer is reflected in a maximum increase in pressure ratio of approximately 5.5% for rotational speeds greater than 26,000 rpm. In conjunction with this, the pressure

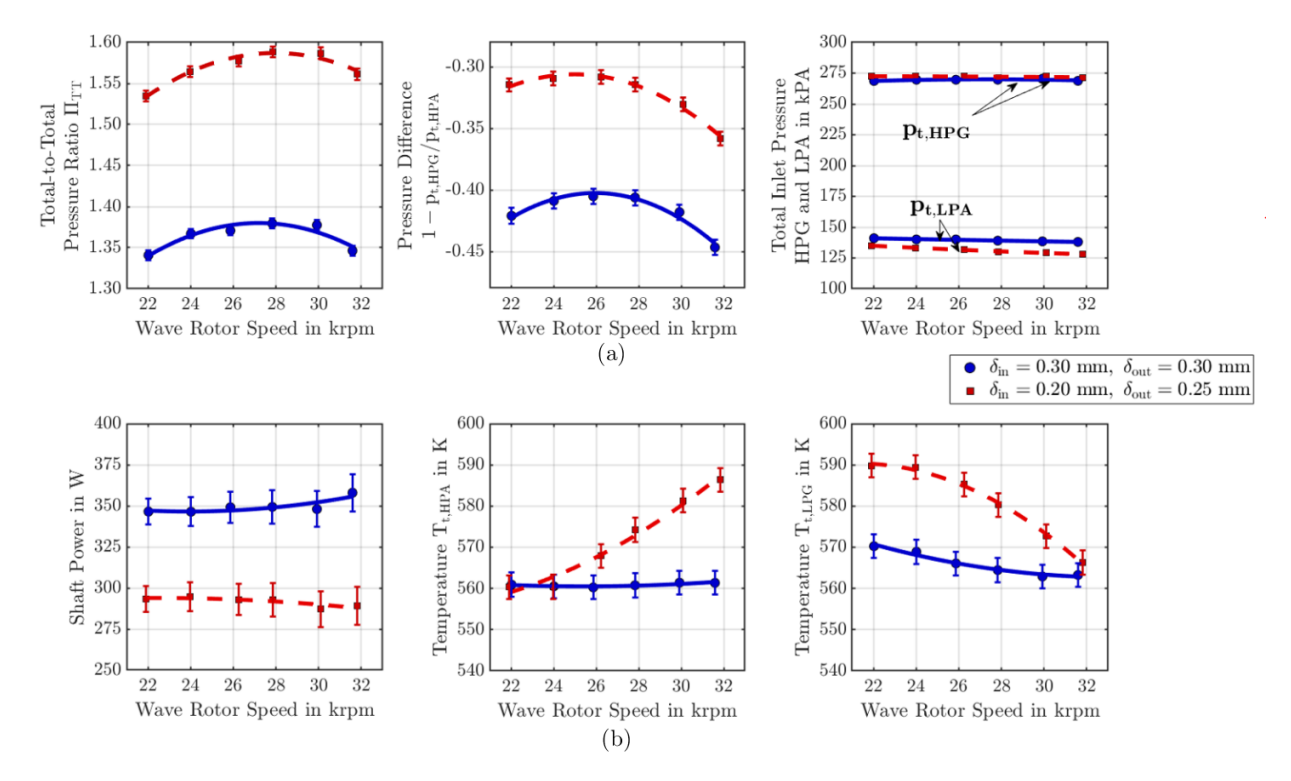


Figure 19: Wave rotor performance data for variations in peak inlet temperature and rotational speed for a nominal axial clearance of 0.3 mm at the in- and 0.3 mm at the outlet side. (a) shows total-to-total pressure ratio (left), (right) and relative pressure difference in the combustor loop between HPG and HPA as well as the total inlet pressure in the LPA inlet, while shaft power output (left) averaged total temperature at HPA (centre) and LPG (right) are shown in (b).

difference across the 'combustor loop', as defined in Figure 4, decreases accordingly.

Impingement of shock and expansion waves on the other end of each wave rotor

channel ideally coincides with opening and closing of the respective ports. Thus, altering wave rotor speed changes the location of impingement and as a consequence the strength the reflected shock wave. This is the reason for the parabolic variation of pressure ratio with wave rotor speed, displayed in the top left graph of Figure 19(a). Furthermore, shaft power output increases can be reported to range within 8% and 3%.

The increase in inlet temperature results in approximately 60°C higher temperature at the outlet throughout all rotational speeds. However, as a consequence of the increased leakage gap - in particular on the outlet side - there appears to be a pronounced interaction among channels and the leakage cavity resulting in a smeared and well-mixed out temperature distribution in both outlets. This effectively

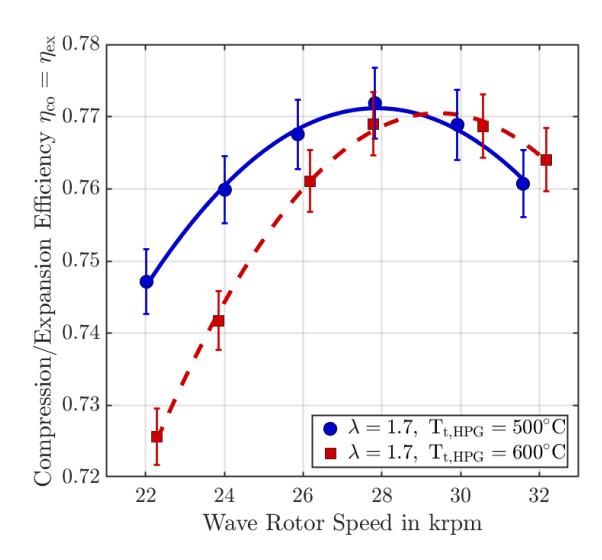


Figure 20: Variation in compression/expansion efficiency with loop flow ratio and rotational speed for two different inlet temperatures at constant axial clearance.

blurs out the effects of FAE and EGR rendering the outlet temperature distribution insensitive to changes in rotational speed, as already described in Figure 17. However, LPG outlet temperature still shows mild sensitivity to rotor speed which hints towards FAE being present at approximately 32,000 rpm. Gas ingestion from the leakage gap and interaction between hot and cold gas streams seem to smear this sensitivity out for the HPA port (centre graph of Figure 19(b)). Nonetheless, the witnessed sensitivity at higher leakage, shown in bottom right graph of Figure 19(b), is reduced compared to lower leakage given in the bottom right distribution shown in Figure 13(b).

The effect of increased peak inlet temperature on compression/expansion efficiency for a loop flow ratio of 1.7 and constant leakage gaps of 0.3/0.3 mm is shown in Figure 20. Despite the increase in compression ratio, as shown in the top left graph of Figure 19(a), no significant change in the efficiency distribution can be reported, except for an slight shift towards higher rotational speeds and a more pronounced drop-off towards lower rotational speeds.

4. Conclusions and Outlook

In this paper a novel four-port, three-cycle small scale wave rotor turbine has been introduced and successfully characterised experimentally on the University of Bath gas stand. In conclusion, the main points of this paper can be listed as follows: • A prototype of the designed rotor was manufactured as a machined-from-solid component and mated with its outer sleeve, while stator components were manufactured using the additive manufacturing based SLM technique. The machine was subsequently installed in a test cell and experimentally tested in an open-loop configuration, where electrical heaters and a set of industrial compressors supply hot and pressurised air. An eddy-current dynamometer was used to measure shaft power output.

- Experimental testing was done with the objective of characterising wave rotor turbine performance through variation of the following parameters:
 - Loop flow ratio λ was varied at fixed hot gas temperature 500°C and nominal clearance gap 0.2 mm inlet, 0.25 mm outlet. The results showed that lower loop flow ratio results in a total pressure ratio increase of around 3% when loop flow ratio is increased from 1.7 to 3.2, although this results in higher pressure difference across combustor loop (connecting the HPG and HPA ports). In addition, outlet temperature increased gradually as a consequence of the reduced cold air mass flow rate. The maximum shaft power output for this test series was around of 450 at loop flow ratio 3.2.
 - Variations in axial leakage comparing results for nominal clearance gap of 0.2 mm at in- and 0.25 mm at the outlet with increased gaps of 0.3 mm at in- and 0.3 mm on the outlet side suggest a significant effect on energy transfer and thus the achieved pressure ratio. Furthermore, increased leakage gap promotes diffusion and mixing of the conditions in neighbouring channels and thus smeared out effects of FAE and EGR.
 - Increasing hot inlet gas temperature from 500°C to 600°C implies an increase in both the attained pressure ratio of around 5% and shaft power increase of 3% to 8%. The increase can be identified as a consequence of the increase in inlet enthalpy.
 - Variations in rotational speed from 22,000 up to the design speed of 32,000 rpm exhibits a parabolic variation of pressure ratio with speed, with the peak pressure being between 28,000 and 30,000 rpm for a loop flow ratio of 1.7. Shaft power shows little sensitivity to rotational speed variation, while outlet temperature implies a decrease in FAE and EGR rate with decreasing rotational speed.
- The test results show that by reducing rotational speed, it is possible to reduce the amount of FAE through the LPG port and decrease EGR rate through

the HPA port. However, the results suggest a conflicting relationship for these parameters with the achieved compression pressure ratio and thus the pressure loss across the HPG and HPA ports. The peak of these parameters lie close to the design speed at approximately 30,000 rpm.

- A method was proposed for computing isentropic efficiency using loop flow ratio as an estimator for EGR rate and taking heat transfer between hot and cold gas streams into consideration. Efficiency computations show high compression/expansion efficiencies in the region of 72% to 82% emphasising the capability of wave rotors to efficiently compress and expand gaseous media.
- Excessive exposure of bearings to heat through hot air ingestion and heat conduction along the shaft limited the peak cycle temperature to 600°C. Future tests shall address this issue through additional seals and more temperature resilient grease being used for bearing lubrication.
- Uneven thermal expansion of rotor as well as in- and outlet stator necessitated using larger axial clearances on both rotor sides. It is further expected that the actual leakage gap varies significantly when the machine is thermal equilibrium. However, determination of the leakage gap in a compact, pressurised and hot environment remains a significant engineering challenge.

Acknowledgement

The authors would like to thank the Defence Science and Technology Laboratory (DSTL) for funding the project under the Defence and Security Accelerator "Beyond Battery Power" competition. The authors would further like to acknowledge the technical staff at the Powertrain and Vehicle Research Centre (PVRC) for their support in setting up the experimental facility as well as researchers Ian Kennedy, Yang Zhang and Tomasz Duda for their support in preparing instrumentation and data acquisition.

References

- [1] R. Nalim, H. Li and P.Akbari, Air-Standard Aerothermodynamic Analysis of Gas Turbine Engines with Wave Rotor Combustion, Proceedings of the ASME Turbo Expo (2009) 445–456.
- [2] P.H. Snyder and M.R. Nalim, Pressure Gain Combustion Application to Marine and Industrial Gas Turbines, Proceedings of the ASME Turbo Expo 5 (2012) 409–422.

- [3] T. Nagashima, K. Okamoto and Y. Ribaud, Cycles and Thermal System Integration Issues of Ultra-Micro Gas Turbines, Educational Notes RTO-EN-AVT-131, 2005.
- [4] P. Akbari, R. Nalim, N. Müller, Performance Enhancement of Microturbine Engines Topped with Wave Rotors, Journal of Engineering for Gas Turbines and Power 128 (2006) 190–202.
- [5] R.D. Pearson, A Gas Wave-Turbine Engine Which Developed 35 HP and Performed Over a 6:1 Speed Range, in: Proceedings ONR/NAVAIR Wave Rotor Research and Technology Workshop, Naval Postgraduate School, 1985.
- [6] B.D. Smith, M.D. Polanka, D.E. Paxson and J.L. Hoke, Scaling Study
 of Wave Rotor Turbo Normalization of an Internal Combustion Engine,
 48th AIAA/ASME/SAE/ASEE Joint Propulsion Conference and Exhibit 2012
 (2012).
- [7] Y. Lei, D.S. Zhou and H.G. Zhang, Investigation on Performance of a Compression-Ignition Engine with Pressure-Wave Supercharger, Energy 35 (2010) 85–93.
- [8] J.Q. Zhao, D.P. Hu, P.Q Liu, F.X. Liu and J.J. Gao, Thermodynamic Analysis
 of a Novel Wave Rotor Refrigeration Cycle, Advanced Materials Research 805 806 (2013) 537–542.
- [9] D.Hu, R. Li, P. Liu and J. Zhao, The Loss in Charge Process and Effects on
 Performance of Wave Rotor Refrigerator, International Journal of Heat and
 Mass Transfer 100 (2016) 497–507.
- [10] H.E. Weber, Shock Wave Engine Design, John Wiley & Sons, New York, 1996.
- [11] P. Akbari, R. Nalim and N. Mueller, A Review of Wave Rotor Technology and
 Its Applications, Journal of Engineering for Gas Turbines and Power 128 (2006).
- [12] G. Lenoble and S. Ogaji, Performance Analysis and Optimization of a Gas
 Turbine Cycle Integrated with an Internal Combustion Wave Rotor, Proceedings
 of the Institution of Mechanical Engineers, Part A: Journal of Power and Energy
 224 (2010) 889–900.
- [13] L. Yani, Z. Dasen, Z. Hongguang, J. Changwei, L. Jiangguo and Z. Tong, Experiment and CFD Investigation of Pressure-wave Supercharger, in: 2008 SAE

- International Powertrains, Fuels and Lubricants Congress, SAE International, 2008.
- [14] M. Mataczynski, J. Hoke, D.E. Paxson and M.D. Polanka, Design, Simulation,
 and Testing of a Pressure Wave Supercharger for a Small Internal Combustion
 Engine, in: SAE 2014 Aerospace Systems and Technology Conference, SAE
 International, 2014.
- ⁶⁷⁷ [15] S. Chan and H. Liu, Mass-Based Design and Optimization of Wave Rotors for Gas Turbine Engine Enhancement, Shock Waves 27 (2017) 313–324.
- [16] F. Klein and S. Staudacher, Plausibility Study of Hecto Pressure Ratio Concepts
 in Large Civil Aero-Engines, Journal of Engineering for Gas Turbines and Power
 140 (2018).
- [17] A. Fatsis, Performance Enhancement of One and Two-Shaft Industrial Tur boshaft Engines Topped with Wave Rotors, International Journal of Turbo and
 Jet Engines 35 (2018) 137–147.
- ⁶⁸⁵ [18] Chan, S. and Liu, H. and Xing, F. and Song, H., Experimental method on the port flow of the wave rotor, 53rd AIAA/SAE/ASEE Joint Propulsion Conference, 2017 (2017).
- [19] K.P. Lapp, M.D. Polanka, M.J. McClearn, J. Hoke and D.E. Paxson, Design
 and Testing of a Micro-Scale Wave Rotor System, in: 53rd AIAA/SAE/ASEE
 Joint Propulsion Conference, AIAA, 2017.
- [20] M.R. Mataczynski, M.J. McClearn, F.R. Schauer, D.E. Paxson and J.L. Hoke,
 Design and Testing of a Small Pressure Wave Supercharger for an Industrial
 Diesel Engine, AIAA SciTech Forum 55th AIAA Aerospace Sciences Meeting
 (2017).
- [21] Haidinger, C. and Kriegler, W. and Millward-Sadler, A. and Eder, P., Feasibility
 and Design Analysis of a Pressure Wave Supercharger Adaption on a 600 cm3
 Spark Ignited Engine, SAE Technical Papers 2017-March (2017).
- [22] J.T. Reinhart, B.A. Beasley, J.L. Hoke, M.J. McClearn and F.R. Schauer, Experimental Observations of a Small-Scale Pressure-Wave Supercharger Coupled to a Compression Ignition Engine, AIAA Aerospace Sciences Meeting, 2018 (2018).

- [23] D.Hu, R. Li, P. Liu and J. Zhao, The Design and Influence of Port Arrangement on an Improved Wave Rotor Refrigerator Performance, Applied Thermal
 Engineering 107 (2016) 207–217.
- [24] J. Zhao and D. Hu, An Improved Wave Rotor Refrigerator Using an Outside
 Gas Flow for Recycling the Expansion Work, Shock Waves 27 (2017) 325–332.
- [25] D. Hu, Y. Yu and P. Liu, Enhancement of Refrigeration Performance by Energy
 Transfer of Shock Wave, Applied Thermal Engineering 130 (2018) 309–318.
- [26] D. Hu, Y. Yu, P. Liu, X. Wu and Y. Zhao, Improving Refrigeration Performance
 by Using Pressure Exchange Characteristic of Wave Rotor, Journal of Energy
 Resources Technology, Transactions of the ASME 141 (2019).
- 712 [27] R.R. Jagannath, S.P.M. Bane and M.R. Nalim, Wave Rotor Combustor Tur-713 bine Model Development, 51st AIAA/SAE/ASEE Joint Propulsion Conference 714 (2015).
- [28] J. Li, E. Gong, L. Yuan, W. Li and K. Zhang, Experimental Investigation on
 Pressure Rise Characteristics in an Ethylene Fuelled Wave Rotor Combustor,
 Energy & Fuels 31 (2017) 10165–10177.
- [29] M.R. Nalim, P.H. Snyder and M. Kowalkowski, Experimental Test, Model Validation and Viability Assessment of a Wave-Rotor Constant-Volume Combustor,
 Journal of Propulsion and Power 33 (2017) 163–175.
- [30] A. Tarraf, R. Ebrahimi, M.E. Feyz and R. Nalim, Application of Response
 Surface Methodology to Investigate the Hot-Jet Ignition of Methane-Hydrogen
 Mixtures in a Constant-Volume Combustor, volume 2017-April.
- [31] S.C. Gülen, Pressure Gain Combustion Advantage in Land-Based Electric Power
 Generation, Journal of the Global Power and Propulsion Society 1 (2017) 288–
 302.
- 727 [32] J. Li, E. Gong, L. Yuan, W. Li and K. Zhang, Experimental Investigation on Flame Formation and Propagation Characteristics in an Ethylene Fuelled Wave Rotor Combustor, Energy & Fuels 32 (2018) 2366–2375.
- 730 [33] H.D. Perkins and D.E. Paxson, Summary of Pressure Gain Combustion Re-731 search at NASA, NASA/TM-2018-219874 (2018).

- ⁷³² [34] J.A.C. Kentfield, The Performance of Pressure-Exchanger Dividers and Equal-⁷³³ izers, Journal of Basic Engineering (1969) 361–369.
- [35] J.A.C. Kentfield, An Examination of the Performance of Pressure Exchanger
 Equalisers and Dividers, PhD Thesis, University of London, 1963.
- [36] J. Wilson and D. Fronek, Initial results from the NASA-Lewis Wave Rotor
 Experiment, AIAA-93-2521 (1993).
- [37] J. Wilson, Design of the NASA Lewis 4-Port Wave Rotor Experiment, Technical
 Report, NASA Contractor Report 202351, 1997.
- [38] J. Wilson, G.E. Welch and D.E. Paxson, Experimental Results of Performance
 Tests on a Four-Port Wave Rotor, NASA/TM2007-214488 (2007).
- [39] M. Mataczynski, D.E. Paxson, M.D. Polanka, and J. Hoke, Performance and
 Design Improvements for a Small Scale Pressure Wave Supercharger, in: 54th
 AIAA Aerospace Sciences Meeting, AIAA SciTech Forum, AIAA, 2016.
- [40] M.J. McClearn, M.D. Polanka, M.R. Mataczynski, F. Schauer, and D.E. Paxson,
 The Design of a Small-Scale Wave Rotor for Use As a Modified Brayton-Cycle
 Engine, in: 52nd AIAA/SAE/ASEE Joint Propulsion Conference, AIAA, 2016.
- [41] M.J. McClearn, M.D. Polanka, M.R. Mataczynski, F. Schauer, and D.E. Paxson,
 The Testing of a Small-Scale Wave Rotor for Use As a Modified Brayton-Cycle
 Engine, in: 52nd AIAA/SAE/ASEE Joint Propulsion Conference, AIAA, 2016.
- [42] R.D. Pearson, Thermodynamics and Gas Dynamics of Internal Combustion
 Engines, Volume II, in: D.E. Winterbone and S.C. Low (Ed.), The Oxford
 Handbook of Innovation, Oxford University Press, Oxford, 1986.
- [43] A. Mathur, Design and Experimental Verification of Wave Rotor Cycles, in:
 Proceedings ONR/NAVAIR Wave Rotor Research and Technology Workshop,
 Naval Postgraduate School, 1985.
- [44] R. Taussig, P. Cassady, J. Zumdieck, W. Thayer and E. Klostermannt, Investigation of Wave Rotor Turbofans for Cruise Missile Engines, Technical Report,
 Final Report Submitted by MSNW to DARPA, 1983.
- [45] J. Piechna and D. Dyntar, Two-Dimensional Numerical Analysis of the Wave Jet
 Micro-Engine Operation, Proc. PowerMEMS 2007 Freiburg, Germany (2007).

- [46] J. Piechna, Feasibility Study of the Wave Disk Micro-Engine Operation, J.
 Micromech. Microeng. 16 (2006).
- [47] J. Piechna and D. Dyntar, Numerical Investigation of the Wave Disk Micro Engine Concept, International Journal of Gas Turbine, Propulsion and Power
 Systems 2 (2008).
- [48] J. Piechna and D. Dyntar, Hybrid Wave Engine Concept and Numerical Simulation of Engine Operation, The Archive of Mechanical Engineering LVII (2010).
- 769 [49] P. Parrage-Ramirez, M. Varney, E. Tarkleson, N. Müller, P. Akbari and J. Piechna, Development of a Wave Disk Engine Experimental Facility, 48th AIAA/ASME/SAE/ASEE Joint Propulsion Conference Exhibit (2012).
- 772 [50] N. Müller, J. Piechna, G. Sun and P.F. Parraga, Wave disc engine apparatus, 773 Patent no. 9,856,791 (2018).
- [51] J. Wilson, G.E. Welch and D.E. Paxson, Experimental Results of Performance
 Tests on a Four-Port Wave Rotor, NASA-TM-2007-214488 (2007).
- [52] Gyarmathy, George, How Does the Comprex Pressure-Wave Supercharger
 Work?, in: SAE International Congress and Exposition, SAE International,
 1983.
- [53] ISO Central Secretary, Measurement of Fluid Flow Procedures for the Evaluation of Uncertainties, Standard BS ISO 5168:2005, International Organization for Standardization, London, UK, 2005.